

Ben-Gurion University of the Negev
The Faculty of Natural Sciences
The Department of Physics

Coherence in the Stern-Gerlach Interferometer

Thesis submitted in partial fulfillment of the requirements for the Master of
Sciences degree

Or Dobkowski
Under the supervision of: Prof. Ron Folman
September 2020

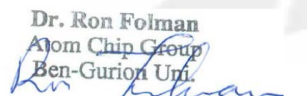
Ben-Gurion University of the Negev
The Faculty of Natural Sciences
The Department of Physics

Coherence in the Stern-Gerlach Interferometer

Thesis submitted in partial fulfillment of the requirements for the Master of
Sciences degree

Or Dobkowski
Under the supervision of: Prof. Ron Folman

Signature of student:



Signature of supervisor:

Signature of chairperson of the committee for graduate studies:

תאריך
Date: 30.9.2020
Date: 30.9.2020
Date: _____
Date: _____

September 2020

Abstract

Interferometers have long been a crucial part in our investigation of nature and physical phenomena. Particularly famous optical interferometer experiments range from Young’s double slit experiment that explored the wave-like nature of light to the Michelson-Morley experiment, and its ultimate extension in the modern era is the Laser Interferometer Gravitational-Wave Observatory (LIGO). Atom interferometers [1] were first developed in the 1990’s, and nowadays are common devices for research in the field of quantum mechanics, and are used in precision measurements of gravity [2], fundamental constants [3], and as accelerometers for inertial guidance and many additional endeavors [4]. While most of these devices make use of the momentum transfer provided by laser pulses to coherently control the paths of an atom, we employ magnetic field gradients [5–7] created by currents in wires on an atom chip. In this thesis I present our realization of the first Stern-Gerlach atom interferometer (SGI), in which the splitting and recombination of quantum wavepackets is performed by forces that arise from magnetic gradients acting upon atomic Zeeman sub-levels.

The Stern-Gerlach effect, discovered a century ago, has become a paradigm of quantum mechanics. Surprisingly there is little evidence that the original scheme with freely propagating atoms exposed to gradients from macroscopic magnets is a fully coherent quantum process. Specifically, no full-loop SGI has been realized with the scheme as envisioned decades ago. Furthermore, several theoretical studies have explained why it is a formidable challenge [8–10]. The recombination in the full-loop SGI is in fact required to be a time-reversal operation of the splitting process, such that the final two magnetic gradients exactly undo the first two. In order to obtain high coherence (or contrast) in the output of a spatial interferometer, one must apply stable and accurate operations on the atom, such that the final relative distance between the wavepackets $\Delta z(2T)$ and the final relative momentum $\Delta p(2T)$ are minimized, where $2T$ is the interferometer duration. Any deviation from complete overlap, either in space or in momentum, will cause a decay in the resulting interferometric contrast. While accuracy is the main challenge, we also need to address the issue of stability, whereby temporal fluctuations may give rise to dephasing. Even in the absence of dephasing, drifts may cause the interference phase to jitter from one experimental shot to the next (e.g., due to a fluctuating bias field), thus smearing the averaged phase, or prevent recombination altogether in the case of noise such as fluctuating gradients.

In Ch. 1 of this thesis I describe the experimental apparatus in our lab including the changes we introduced during the time of this work.

Ch. 2 describes the experimental procedure for achieving a Bose-Einstein condensation (BEC) and the steps manipulating the atomic states which make up the sequence of the SGI.

In Ch. 3 the theoretical background of atom interferometry is presented, mainly discussing the visibility and the phase of the full-loop SGI.

Ch. 4 presents our realization of the full-loop SGI, confirming successful active recombination achieved by the two final magnetic gradients. We also confirm the prediction for the phase of the SGI and its dependence on the final spatial separation of the wavepackets. Finally, we present a measurement of the coherence length of the wavepacket in the SGI.

In Appendix A we discuss the effect of shot-to-shot phase fluctuations on the experimental signal, and suggest a protocol to estimate the noise sources affecting the phase stability.

Publications

O. Amit, Y. Margalit, O. Dobkowski, Z. Zhou, Y. Japha, M. Zimmermann, M. Efremov, F. Narducci, E. Rasel, W. Schleich, and R. Folman, “ T^3 Stern-Gerlach Matter-Wave Interferometer”, Phys. Rev. Lett. **123**, 083601 (2019).

M. Keil, S. Machluf, Y. Margalit, Z. Zhou, O. Amit, O. Dobkowski, Y. Japha, S. Moukouri, D. Rohrlich, Z. Binstock, Y. Bar-Haim, M. Givon, D. Groswasser, Y. Meir, and R. Folman, “Stern-Gerlach Interferometry with the Atom Chip”, arXiv:2009.08112 (2020).

Y. Margalit, O. Dobkowski, Z. Zhou, O. Amit, Y. Japha, S. Moukouri, D. Rohrlich, A. Mazumdar, S. Bose, C. Henkel, and R. Folman, “Realization of a complete Stern-Gerlach Interferometer: Towards a Test of Quantum Gravity”, in preparation (2020).

“Separation Phase in a Stern-Gerlach Interferometer”, in preparation (2020).

“Geometric effects in a Stern-Gerlach Atom Interferometer”, in preparation (2020).

Acknowledgments

My M.Sc. work described in this thesis has been a journey into the world of experimental physics, and I would like to express my appreciation for the people who were part of this journey.

I would like to thank Prof. Ron Folman, my research supervisor, for his guidance and support, both in my academic endeavors and personal life, and for reaching out to help when I really needed it.

Thanks to Dr. Mark Keil for mentoring me in writing this thesis, keeping my progress on schedule, making sure I use proper English and notations, and lifting my spirits.

Thanks to Dr. Yoni Japha for long discussions, endless patience, and the supporting theoretical work for our experiment.

Thanks to Dr. David Groswasser, for building the lab, helping with challenges in our apparatus and especially for the hard work on the main power supplies of the lab, which was crucial for the success of our experiment.

I would like to express my very deep appreciation to my colleague and mentor Dr. Yair Marglit for accepting me into the BEC2 team, teaching me all about our experimental work and traditions, and the many conversations after moving to the U.S., and to Dr. Shimon Machluf who built the BEC2 system. Many thanks to Omer Amit who worked with me on the experiment, for the many hours of joint work, interesting discussions, and the dedicated work while we were fixing and improving the system. Many thanks to Dr. Zhifan Zhou for the opportunity to work together and the many night shifts of data taking we did together.

To Zina Binshtock: thanks for being a master of electronics and building any special equipment we needed for the experiment. My gratitude to Yaniv Bar-Haim for his careful attention to the lab and being a friend. I would like to thank the rest of the Atom-Chip group with whom I had the pleasure of working: Daniel, Guobin, Hezi, Ketan, Meni, and Samuel. To Tuval Ben Dosa, thanks for writing the code for interfacing our software with the M-loop algorithm, a daunting task that you performed outstandingly.

Finally, I wish to thank my family; my parents for their support and encouragement in life, my two sisters for their friendship, my spouse Dafna for the care and patience and cheering me up, and our newborn child who is still waiting for his father to finish his thesis so he can finally get a name.

Contents

Introduction	i
Publications	ii
Acknowledgments	iii
List of Figures	vi
Abbreviations	vii
1 The experimental apparatus	1
1.1 Vacuum system	1
1.2 Magnetic fields	1
1.3 Laser system	1
1.4 Imaging system	2
1.5 The atom chip	3
1.6 Introduced changes, checks, and upgrades to the apparatus	4
2 The experimental procedure	5
2.1 Trapping and cooling the atoms	5
2.1.1 Magneto-optical trap	5
2.1.2 Preparation for the magnetic trap	7
2.1.3 Magnetic trap	8
2.1.4 Evaporative cooling	9
2.1.5 Bose-Einstein condensation	9
2.2 Manipulating the atoms	10
2.2.1 Initial position – changing the trap position	10
2.2.2 Initial state – cleaning residual $m_F = 1$	10
2.2.3 Internal state manipulation	11
2.2.4 Population measurement	12
2.2.5 Stern-Gerlach splitting using the atom chip	13
2.3 Troubleshooting a complex experimental procedure	14
3 Atom Interferometry	17
3.1 Interferometry in the history of physics	17
3.2 Stern-Gerlach Interferometer (SGI)	17
3.2.1 Half loop – spatial fringes	18
3.2.2 Full loop SGI – spin population fringes	18
3.3 Phase of the SGI	19
3.3.1 The action difference	20
3.3.2 Separation phase of an open SGI	21

3.4	Visibility of the full-loop SGI	22
3.4.1	Experimental measurement of visibility	22
3.4.2	Theoretical prediction of the visibility	22
3.4.3	Generalized wavepacket model	23
4	Implementation of the full-loop Stern-Gerlach Interferometer	26
4.1	Experimental sequence	26
4.2	Results	28
4.2.1	Coherence and splitting	28
4.2.2	Demonstrating active recombination	29
4.2.3	Coherence length	29
4.2.4	Momentum coherence width	31
4.2.5	Momentum coherence width and temperature	32
4.3	Phase noise	32
5	Summary and Outlook	34
	Appendices	39
A	Phase noise analysis	40
A.1	Phase noise simulation	40
A.1.1	Model	40
A.1.2	Measuring the shot-to-shot phase stability	41

List of Figures

1.1	Copper structure and chip mount	2
1.2	BGU2 atom chip	3
1.3	Temperature logger	4
2.1	^{87}Rb energy level structure for the D_2 line	6
2.2	Light and magnetic fields in a MOT in one dimension	7
2.3	Atoms in the magneto-optical trap	8
2.4	BEC in free fall	10
2.5	Bloch sphere representation of a two-level system	12
2.6	Ramsey and spin-echo sequences	13
2.7	Quadrupole field of the atom chip and its advantages	15
4.1	Experimental sequence for the full-loop SGI	27
4.2	SGI optimization procedure	28
4.3	Experimental sequence and timing, full-loop and double kick	29
4.4	Effective recombination in the SGI and phase of the SGI	30
4.5	Single kick effect on the visibility	31
4.6	Number of atoms and cloud size vs. last RF ramp	32
4.7	Momentum coherence width and temperature	33
A.1	Two noisy population measurements	40
A.2	Simulated shot-to-shot phase fluctuations	44
A.3	Noise in population vs. phase noise, numerical simulation	45
A.4	Phase scan with shot-to-shot noise, numerical simulation	46
A.5	Population vs. Ramsey time, experimental data vs. numerical simulation	47
A.6	Goodness of fit vs. field stability	48

Abbreviations

MOT	magneto-optical trap
AOM	acousto-optic modulator
BEC	Bose-Einstein condensate
GP	Gross-Pitaevskii
OD	optical density
SG	Stern-Gerlach
SGBS	Stern-Gerlach beam-splitter
SGI	Stern-Gerlach interferometer
TF	Thomas-Fermi
TOF	time-of-flight
NMR	nuclear magnetic resonance

Chapter 1

The experimental apparatus

The experimental apparatus was built during the years 2007-2008, with some important changes over the years, mainly replacing the atom chip, the main laser and peripheral electronics. A detailed description of the apparatus is given in the PhD thesis of Shimon Machluf, who built the system [11] with the assistance of Dr. Plamen Petrov, a Post-Doctoral Fellow in the Atom Chip Group. This chapter briefly describes the apparatus consisting of a vacuum system; coils and copper structures for creating magnetic fields; laser system for cooling, trapping and imaging the atoms; and the atom chip on its mount that creates the required magnetic potentials and gradients. While the setup was mainly constructed before my time, I detail at the end of the chapter several changes and improvements I have implemented (together with Omer Amit) during my M.Sc.

1.1 Vacuum system

The vacuum system did not change during this work. It is built around a 6-way cross to which all other vacuum parts are connected. The frame is designed to hold the vacuum system and magnetic coils rigidly, with as few vibrations as possible, but still with enough space to enable easy access from all directions. At the bottom of the 6-way cross we connect the science chamber and from the top we insert the mount with the atom chip. On two of the sides we have the turbo-molecular pump and the ion pump. The turbo pump can reduce the pressure to $\sim 10^{-8}$ Torr, and the ion pump can reduce the pressure to $\sim 10^{-11}$ Torr. We occasionally use a titanium sublimation pump which coats the chamber walls with titanium to absorb some of the residual gas particles thereby helping the ion pump.

1.2 Magnetic fields

We use three pairs of Helmholtz coils producing the x , y and z bias fields required for trapping and cooling the atoms. The G/A ratio (magnetic field per unit current) of the magnetic coils was measured in [12] to be (0.835, 0.834, 1.007) G/A for the (x, y, z) coils. The potentials for the magneto-optical trap (MOT) and magnetic trap are produced by currents through a copper structure inside the science chamber just beneath the chip surface, in the shape of U and Z wires (Fig. 1.1). Home-made current shutters are used for fast switching of the currents.

1.3 Laser system

Four laser frequencies are required in the experiment for cooling, repumping, optical pumping, and imaging the atoms. We achieve this with two lasers and four acousto-optic modulators (AOMs). The main laser is a Toptica TA 100, which delivers up to 1000 mW of power; we work at an output

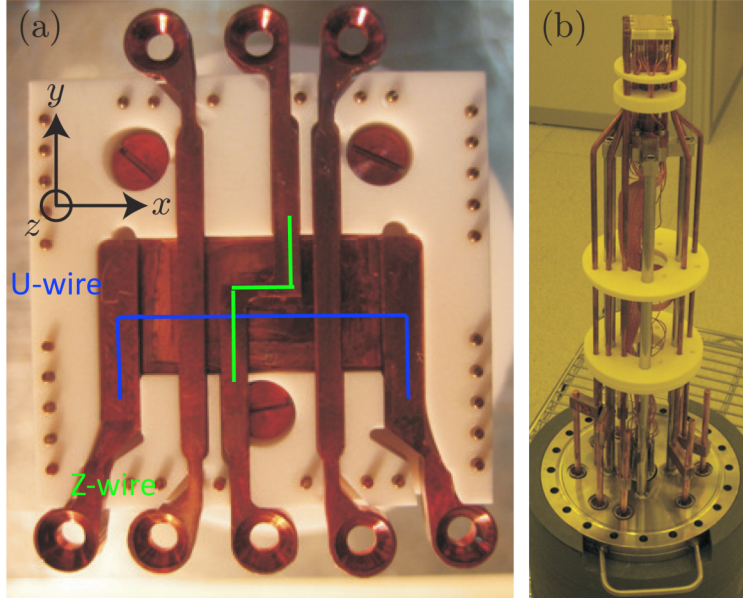


Figure 1.1: Copper structure and chip mount. (a) The copper structure: the U-wire produces the inhomogeneous magnetic field for the MOT, and the Z-wire produces the magnetic potentials for the magnetic trap. (b) The chip mount with the chip on top of it. The mount is inserted upside down so that the chip is facing downwards inside the science chamber.

of 850 mW which is enough. The beam is split into three different frequencies for cooling, optical pumping and imaging, each passing through a different AOM. The secondary laser is home-made and can deliver ~ 40 mW; it is used as a repumper during the MOT. We lock the frequency of both lasers on a polarization spectroscopy signal using a rubidium vapor cell and a PID circuit. All four beams are coupled into optical fibers and transferred to the science chamber, and each beam is blocked by a mechanical shutter (Uniblitz LS6) while not in use during parts of the experimental cycle.

1.4 Imaging system

We use on-resonance absorption imaging throughout this work. The system consists of a CCD camera, lenses, and the imaging laser beam. Two lenses of focal lengths 200 mm and 300 mm magnify the image of the atoms by a factor $3/2$. The camera is a Prosilica GC2450 with Sony ICX625 CCD sensor, and a pixel size of $3.45 \mu\text{m} \times 3.45 \mu\text{m}$, which results in a pixel size of $2.3 \mu\text{m} \times 2.3 \mu\text{m}$ in the object plane. The imaging resolution is diffraction limited; the numerical aperture (NA) of 0.126 yields a diffraction limit of $\lambda/(2\text{NA}) = 3.1 \mu\text{m}$. This resolution was confirmed experimentally as described in [13]. The imaging beam is tuned to the $F = 2 \rightarrow F' = 3$ transition. To get an absorption image we apply two separate imaging laser pulses; the intensity of the beam with atoms and without the atoms, $I(x, z)$ and $I_0(x, z)$, are recorded by the CCD. The atomic density can be extracted using the Beer-Lambert law

$$I(x, z) = I_0(x, z) \exp[-\text{OD}(x, z)], \quad (1.1)$$

where OD is the optical density and $I(x, z)$, $I_0(x, z)$ are the CCD pixel intensities in the imaging plane with and without atoms respectively. The optical density is proportional to the column density of the atoms at a given position $\int n(x, y, z) dy$, where x and z are the object plane positions and the imaging laser is incident along the y -axis. The number of atoms $N(x_i, z_j)$ imaged by a

pixel is

$$N(x_i, z_j) = \frac{A}{\sigma_o} \text{OD}(x_i, z_j), \quad (1.2)$$

where A is the pixel area in the object plane, $\sigma_o = 3\lambda^2/2\pi$ is the cross-section for resonant atom-light scattering for atoms in the $m_F = 2$ Zeeman sub-level with σ^+ polarized light, and $\lambda \approx 780.241$ nm is the optical transition wavelength for the the D₂ electronic transition, ($5^2S_{1/2} \rightarrow 5^2P_{3/2}$) of ^{87}Rb [14].

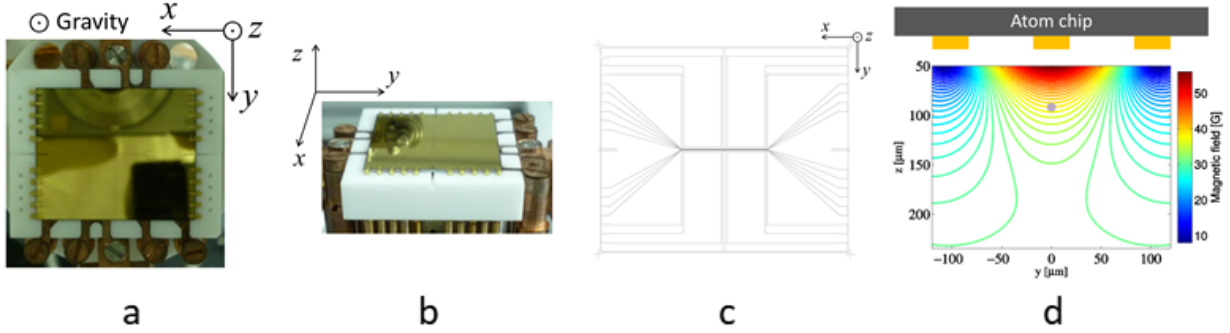


Figure 1.2: BGU2 atom chip. (a) Top view, showing the chip on its mount, with the copper wire structure partially covered by the atom chip. The chip faces downwards in the science chamber and the atoms are trapped $\sim 100 \mu\text{m}$ below the chip. (b) Side view, in which the bonding wires and pins for the electrical connections to wires can be seen. (c) Design of the BGU2 atom chip. The chip size is $25 \text{ mm} \times 30 \text{ mm}$. There are five 10 mm -long wires in the middle of the chip, three of which are used in the experiment to create the 2D quadrupole field. (d) Magnetic field strength below the atom chip, generated by the three chip wires and a homogeneous bias field B_y . The wires are represented by the gold rectangles below the chip and the gray dot represents the position of the trapped atoms. The current in the central wire is in the opposite direction to the currents in the adjacent wires. The magnetic field in the proximity of the central wire is stronger than in the proximity of the two adjacent wires because the magnetic field below the central wire is pointing in the same direction as the bias field B_y while the magnetic field below the two adjacent wires is pointing in the opposite direction. This effect will be reversed if the polarity of the currents is reversed.

1.5 The atom chip

Coherent momentum splitting using magnetic gradients [5] requires accurate and strong magnetic gradients, with short pulses of those gradients. To create the desired magnetic gradients, we use an atom chip. Brief current pulses through the chip’s micro-fabricated wires create accurate and strong gradients, and the low inductance of the chip allows short current pulses. The atom chip consists of a silicon wafer covered with gold, where insulating gaps in the gold layer define the wires. The fabrication of the chip was done in an advanced fabrication facility¹ capable of producing complex structures accurately, which in turn form the required magnetic potentials. The atom chip in the apparatus is the “BGU2” atom chip (Fig. 1.2); a detailed description of this chip is given in [13]. For a thorough review of atom chips, see [15].

The strong magnetic gradient required for the experiment can be achieved with one straight wire, but we use an improved design with three parallel wires (note that the chip has 5 parallel wires but the two outermost wires are not needed for the experiments described in this thesis). The wires are 10 mm long, $40 \mu\text{m}$ wide, and $2 \mu\text{m}$ thick. The wire centers are separated by $100 \mu\text{m}$, and the same current runs through them but in alternate directions, creating a 2D quadrupole

¹The BGU2 atom chip was produced at Ben-Gurion University of the Negev in The Weiss Family Laboratory for Nano-scale Systems (<http://in.bgu.ac.il/en/nano-fab/Pages/default.aspx>).

field at $z = 100 \mu\text{m}$ below the atom chip. Positioning the atoms near the zero of the quadrupole significantly improves the stability of the Stern-Gerlach interferometer (SGI), as the phase noise is largely proportional to the magnitude of the magnetic field during the gradient pulse. The improved phase stability is discussed and demonstrated in detail in [7]. As a power supply for the chip we use simple 12 V batteries, and turn the current on/off using solid-state current shutters that allow pulses as short as $1 \mu\text{s}$.

1.6 Introduced changes, checks, and upgrades to the apparatus

I present here a list of changes and upgrades to the apparatus. We installed the Toptica TA 100 in April 2019 after the Toptica DLX110 had a malfunction; the TA 100 was the main laser in the first BEC experiment in our lab and is ~ 15 years old. After installing it, the Toptica TA 100 laser showed some instability, drifting from single-mode operation to multi-mode over time; the extra modes reduced the number of atoms in the MOT, which prevented us from getting a BEC. To monitor this problem we installed a Fabry-Pérot interferometer and monitored the laser modes daily. This problem was finally solved by replacing the old laser diode with a new one.

The original mechanical shutters were home-made from loudspeakers, and were replaced with commercial Uniblitz LS6 shutters. The commercial shutters have a shorter response time, which means adjustment of the trigger timing was required after changing the shutters. We implemented a machine-learning online optimization algorithm [16] into our experimental control, and successfully tested it on simple optimizations in a one-parameter space. We built a home-made, Arduino based, temperature logger that monitors and records the temperature of 7 points in the apparatus (see Fig. 1.3). This was done as part of the effort to better understand the apparatus and improve its stability.

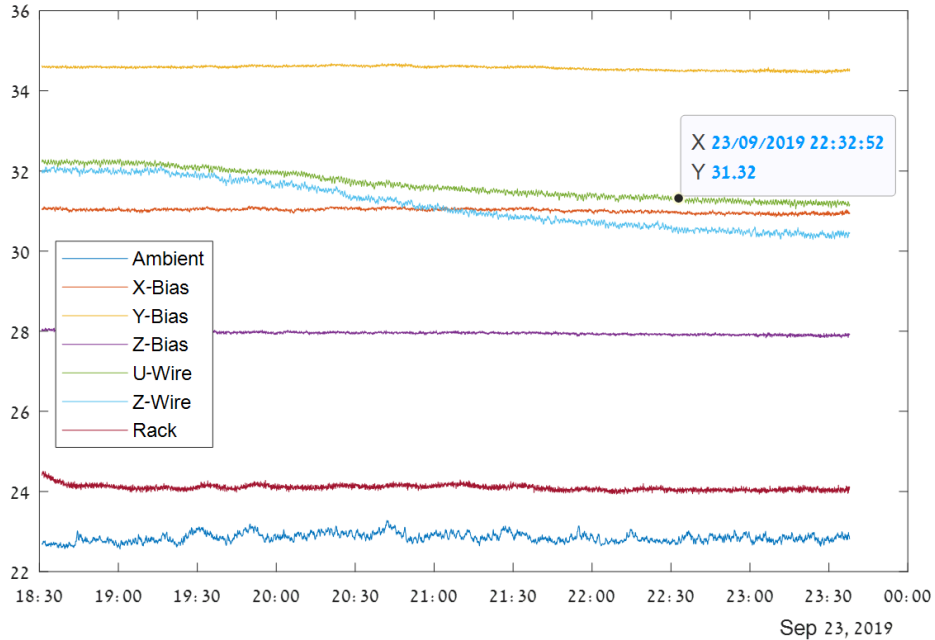


Figure 1.3: Temperature logger: home-made, Arduino based, temperature logger measures the temperature at 7 points of the apparatus. The data is recorded to a text file, and later loaded into Matlab to produce a plot of temperature vs. time.

Chapter 2

The experimental procedure

Following the previous chapter in which I described the apparatus, here I describe the experimental procedure. The experimental cycle is 1 minute long, the first 32 seconds of which are required to trap and cool the atoms to a Bose-Einstein condensate (BEC), with just a few milliseconds required for the interferometric sequence. The rest of the cycle allows the coils and copper structure to cool down so that all cycles start at the same temperature. Producing the BEC begins with a magneto-optical trap (MOT), then loading the atoms into a magnetic trap and performing evaporative cooling. The interferometric sequence is performed while the atoms are in free-fall during which time we manipulate the internal state of the atoms using RF pulses and control the position and momentum of the atoms using magnetic gradient pulses originating from the atom chip. This chapter describes each stage of the experimental procedure up to the interferometric stage (more details can be found in the theses of Tal David [17], Ran Salem [18] and Shimon Machluf [11]), while the following chapters detail the theory and practice of our Stern-Gerlach interferometry experiments. As in Ch. 1, I end the chapter with an account of my own contributions to the experimental procedure.

2.1 Trapping and cooling the atoms

2.1.1 Magneto-optical trap

The MOT consists of magnetic fields from two sets of Helmholtz coils, combined with the U-wire quadrupolar magnetic field, and four red-detuned laser beams arranged in a “mirror-MOT” configuration [19]. The atoms slow down as they experience a drag force due to the interaction with a red-detuned laser, such that the Doppler shift allows the atoms to absorb a photon and receive a recoil only against their direction of movement. This drag force is in fact a friction force as it is velocity dependent, and consequently the atoms cool down. To trap the atoms and increase their density, a position-dependent force is also required, and is achieved by use of magnetic fields (quadrupole configuration) in addition to the light fields noted previously. The transition resonance frequency changes with the magnetic field, due to the Zeeman splitting $\Delta E(r) = -\mu_B m_F g_F B(r)$, thus making the interaction probability with the laser position-dependent. With the correct configuration of magnetic fields and light polarization, a restoring force due to recoil from the laser beams will act on the atoms, thus trapping them in the center of the quadrupole field (see Fig. 2.2). The magnetic fields are produced by a current of 50 A in the U-shaped wire, and homogeneous bias fields of ~ 5 G and ~ 1 G in the y and z directions, respectively (see Fig. 1.1). Rubidium atoms are released into the science chamber by running a current of 12 – 17 A through a pair of dispensers wired in parallel. The dispensers are shut down after 12s while keeping the lasers and fields on, keeping the atoms trapped in the MOT, allowing the background gas to be pumped and the pressure in the science chamber to drop, thereby increasing the lifetime of atoms in the magnetic trap which follows and in which the evaporative cooling will take place. In the MOT, each laser beam has two

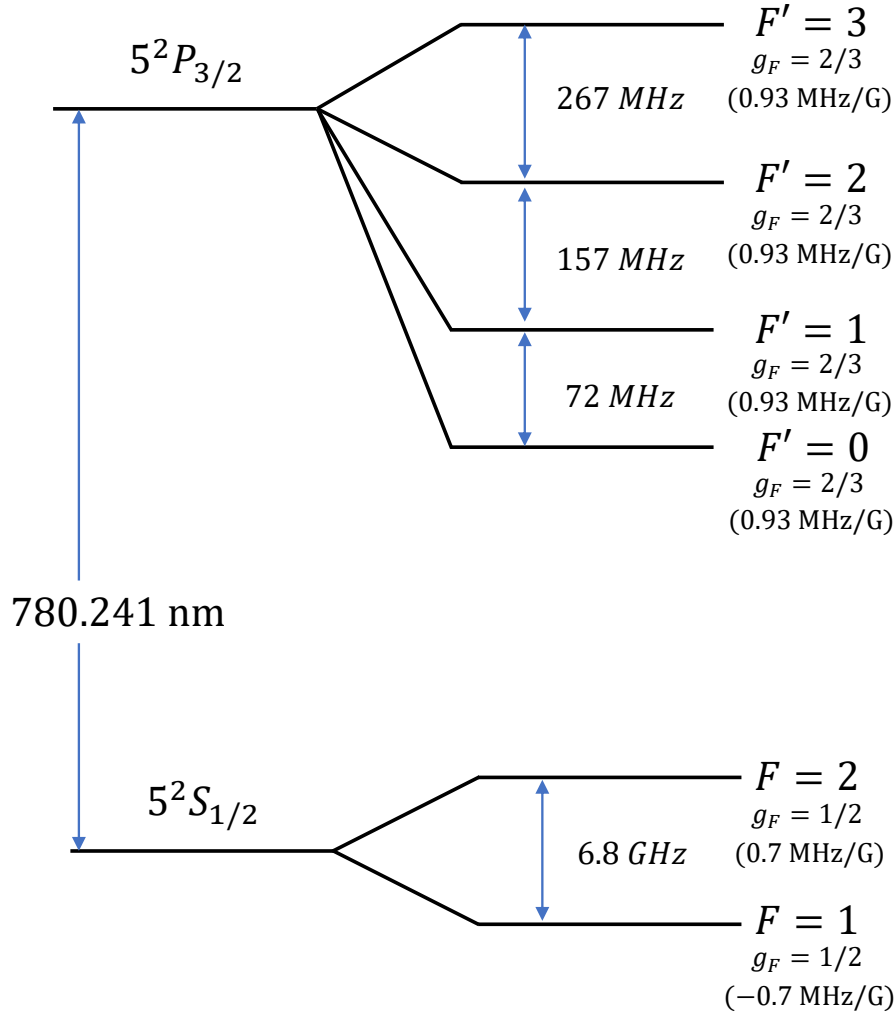


Figure 2.1: ^{87}Rb energy level structure of the D_2 line. The fine-structure splitting occurs because of the electron spin - orbital momentum interaction ($L \cdot S$), while the hyperfine structure results from the interaction of the nuclear angular momentum and the electronic total angular momentum ($I \cdot J$). Each hyperfine level is further split into $2F + 1$ states because of the Zeeman interaction. Before loading to the magnetic trap we optically pump the atom to the $|F = 2, m_F = 2\rangle$ state, as the trappable Zeeman sub-levels in the $F = 2$ manifold are $m_F = 1$ and 2.

different frequencies, one for cooling and the other for repumping. The cooler is $\sim 3\Gamma = 18 \text{ MHz}$ red-detuned from the $F = 2 \rightarrow F' = 3$ transition (Γ is the electronic transition linewidth). This cooling transition can be repeated many times since it is a closed cycle: an atom in the excited $F' = 3$ state can only decay to the $F = 2$ ground state. However, some of the atoms ($\sim 1/300$) go through the $F = 2 \rightarrow F' = 2$ transition due to the finite width of the transition, and these atoms can decay to the $F = 1$ ground state and be lost from the cooling cycle. Since this will happen once for every 1000 transitions, and each atom is excited every $\sim 26 \text{ ns}$, all the atoms will be in the $F = 1$ ground state in $\sim 26 \mu\text{s}$. The repumper laser is therefore tuned to the $F = 1 \rightarrow F' = 2$ transition, from which the atoms can decay to $F = 2$ and return to the cooling cycle.

In November 2019 we suspected the dispensers are starting to degrade as we couldn't get a BEC. To improve the number of atoms in the MOT without significantly increasing the background

pressure, we added ultra-violet (UV) LEDs shining through the bottom window of the science chamber. This releases atoms from the windows and surfaces which significantly improved the fluorescence signal of the MOT and the number of atoms in the BEC. In contrast to the dispensers, shutting down the UV light immediately stops the release of atoms to the science chamber allowing the LEDs to run longer; we found that the optimal run time for the UV LEDs is 19 s. The number of atoms in the MOT is around $50 - 60 \cdot 10^6$; Fig. 2.3 shows a picture of the MOT.

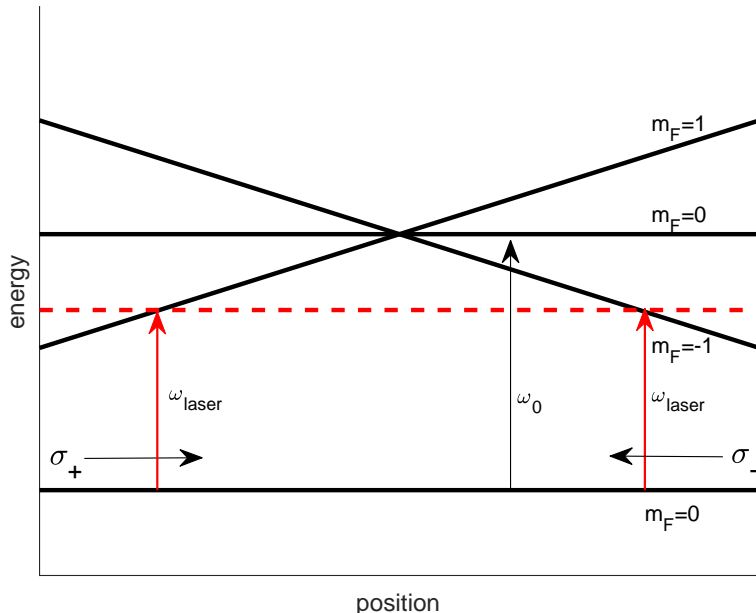


Figure 2.2: Light and magnetic fields in a MOT in 1 dimension for an idealized $F = 0 \rightarrow F' = 1$ two-level system (in the lab frame). The horizontal dashed line is the laser light frequency, ω_{laser} which is detuned from the resonance frequency of the atomic transition, ω_0 . The energies of the excited states, $m_F = 0, 1, -1$ are marked by solid lines, with different Zeeman energies due to the position dependence of the quadrupolar magnetic field. Two counter-propagating laser beams, with polarization σ_+, σ_- are directed at the atoms. The probability of absorbing a σ_+ photon is maximal when the laser frequency matches the transition frequency from the ground state $m_F = 0$ to the excited state $m_F = 1$, thus the force acting in the two directions is not balanced and an effective restoring force is applied to the atoms (adapted from [20]).

2.1.2 Preparation for the magnetic trap

To load atoms into the magnetic trap the atoms must be cold enough and located in a volume overlapping the trap, as well as being in a trappable state. This is achieved by compressing the MOT, further cooling via a gray MOT and optical molasses, and finally applying optical pumping to bring the atoms to a magnetically trappable state. In our case, we use the trappable low-field seeking $|F, m_F\rangle = |2, 2\rangle$ state. The MOT is much larger than the magnetic trap, so loading the atoms directly from the MOT to the magnetic trap would be inefficient. To improve the efficiency of loading we compress the MOT and move it closer to the chip by changing the magnetic fields. The current in the U-shaped wire is increased from ~ 50 A to ~ 75 A and the bias field in the y -axis is increased from 5 G to 24 G so that the position and size of the MOT is as close as possible to those of the magnetic trap. This process is called mode matching and is optimized so that the number of atoms loaded to the magnetic trap is maximal. The compression is done adiabatically in 100 ms. Further cooling is done in two steps, gray MOT and molasses. In the gray MOT, the cooler detuning is increased to $\sim 6\Gamma$, while keeping the magnetic fields on. The magnetic fields are turned off for the molasses stage, and the detuning is further increased, bringing the temperature of the atoms at the end of the molasses to $\sim 150 \mu\text{K}$. At the end of the molasses the atoms are in

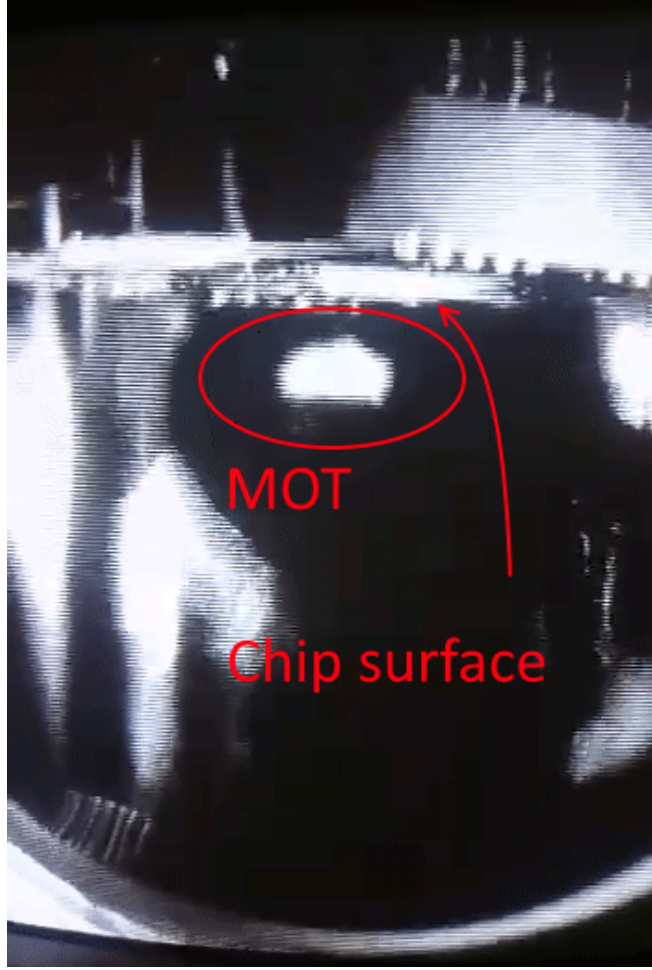


Figure 2.3: Atoms in the magneto-optical trap, a few millimeters below the chip surface, taken with a black-and-white CCD camera and a CCTV. The atoms fluoresce due to scattering of the laser light. The chip surface, Macor base and wire bonding are visible.

$F = 2$, distributed evenly over all five Zeeman sub-levels. We apply a short pulse of σ_+ polarized laser beam along the y -axis, while a bias field in the y -axis provides the quantization axis. This optical pumping beam is tuned to the $F = 2 \rightarrow F' = 2$ transition; repeated excitation-emission cycles fully polarize the atoms in the $|2, 2\rangle$ state, from which no further laser excitation is possible. Some atoms can decay to $F = 1$, so the repumper is also turned on during the optical pumping stage.

2.1.3 Magnetic trap

Magnetic trapping of neutral atoms is based on the interaction of the magnetic moment of the atom μ with the magnetic field B , of the form:

$$U = -\boldsymbol{\mu} \cdot \mathbf{B} \approx m_F g_F \mu_B |\mathbf{B}|, \quad (2.1)$$

where m_F is the projection of the total atomic angular momentum F on the quantization axis (the magnetic field in our case), g_F is the Landé factor, μ_B is the Bohr magneton, and $|\mathbf{B}|$ is the magnitude of the magnetic field. This is the Zeeman interaction and it lifts the degeneracy of the different m_F states, which are named the Zeeman sub-levels.

Magnetic trapping of neutral atoms was first demonstrated in 1985 by Migdall *et al.* [21], using a quadrupole trap consisting of two coils in an anti-Helmholtz configuration. The trap depth was

~ 17 mK, the trap lifetime was 0.87 s, limited mainly due to collisions with background gas. In a quadrupole trap the magnetic field at the center is zero, causing a degeneracy between the trapped and untrapped states, and consequently allowing the atoms to flip their spin orientation and get pushed out of the trap, known as Majorana spin flips. To prevent atom loss due to Majorana spin flips, we use a Ioffe-Pritchard trap with a non-zero minimum lifting the degeneracy. The trap is created by a right-angled Z-shaped wire (see Fig. 1.1a) carrying a current of 90 A combined with a bias field of 50 G along the y -axis [22]. We also use an x -axis bias field of 33 G to lower the magnetic field at the trap bottom. The trap has radial frequencies in the y and z directions of $2\pi \times 585$ Hz and an axial (longitudinal) frequency of $2\pi \times 40$ Hz, and is ~ 400 μ m below the atom chip. After loading to the magnetic trap we have $30 - 40 \cdot 10^6$ atoms in the trap, the temperature of the cloud is ~ 300 μ K, and the position is ~ 2.5 mm below the atom chip. Once the atoms are loaded into the trap we start the evaporative cooling.

2.1.4 Evaporative cooling

After the atoms are loaded into the magnetic trap, we start the evaporative cooling stage, where we use RF radiation to selectively expel hot atoms from the trap [23]. This so-called RF knife couples the trapped Zeeman sub-levels to untrapped sub-levels and the atoms in such untrappable states are expelled from the trap. The inhomogeneous field of the magnetic trap leads to an energy-selective loss of atoms, whereby only the hot atoms, which make it to the far edges of the trap where there is a significant magnetic field, are in resonance with the RF field. As a result, the remaining atoms are re-thermalized by means of elastic collisions and the mean temperature of the atomic cloud decreases. The RF frequency starts at 50 MHz and is exponentially lowered within 12 s in a series of steps to a final value of ~ 0.6 MHz (we use values in the range of $\sim 0.4 - 0.6$ MHz depending on the value of the x -axis bias field). The lowest RF frequency, which controls the final cloud temperature and BEC purity, is optimized from time to time, to compensate for minor changes in the magnetic fields.

2.1.5 Bose-Einstein condensation

One characteristic of a BEC is the anisotropic expansion it exhibits in free-fall after being released from the trap. Fig. 2.4 shows a series of images of a BEC for increasing time-of-flight (TOF) after trap release. The cloud is falling freely with gravity and expands faster in the radial y and z directions, exhibiting in the imaging x - z plane an anisotropic expansion mainly in the vertical (z) direction. For non-interacting atoms this anisotropy can be explained using the uncertainty principle, as the BEC is a minimal uncertainty state and the shape of the cloud after TOF reflects its initial momentum distribution, so the smaller dimension of the cloud expands faster. For interacting atoms such as those used in our experiment, the Gross-Pitaevskii equation (GPE) [24] predicts a repulsive force $F \propto -\nabla n(r)$, where $n(r)$ is the density distribution of the BEC. This repulsive force is stronger in the radial direction due to the cloud's initial shape due to the trap frequencies detailed above. The expansion due to the interaction energy has the same characteristics as those due to the uncertainty principle but they are typically stronger and the contribution due to the uncertainty principle can be neglected. At the end of the RF evaporation we have $\sim 10^4$ atoms in the BEC state. The evaporation can be stopped above or below the transition temperature to BEC, thus controlling the relative number of atoms in the condensate; we usually begin our experiments with a purity of $\sim 70\%$.

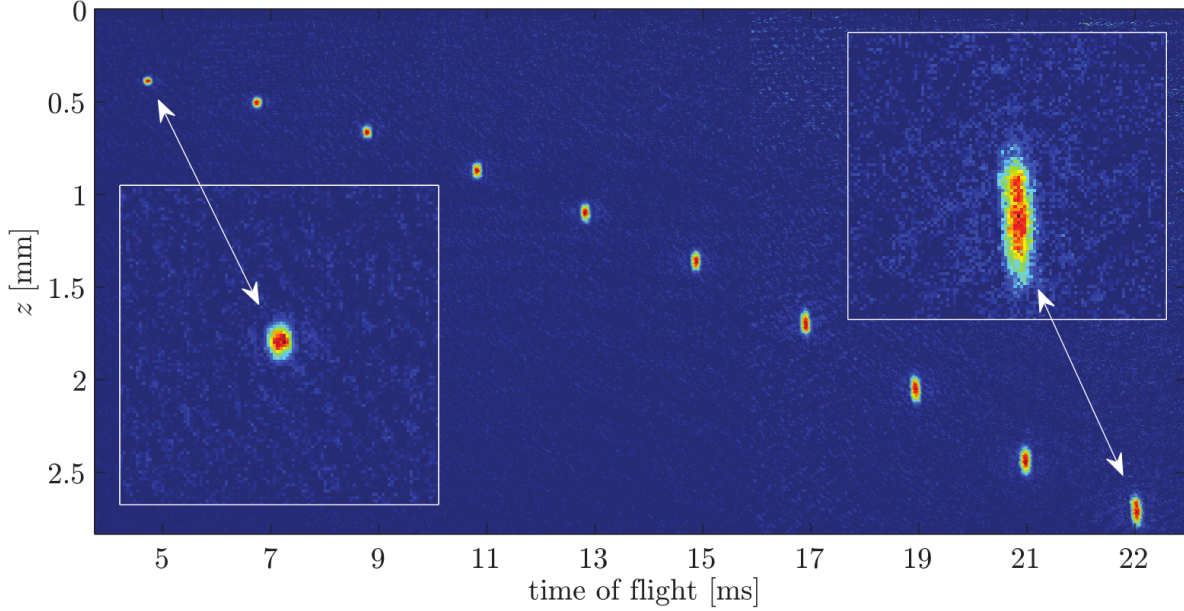


Figure 2.4: Images of a freely-falling BEC taken for different TOF (time-of-flight). The shape of the BEC is changing and exhibits anisotropic expansion. At trap release (TOF=0) the cloud is elongated in the horizontal (x) direction (not shown due to imaging limitations), reflecting the trap orientation, but it expands faster on the vertical axis so that after 5 ms it is fairly symmetric and after 22 ms it is elongated in the vertical z -axis as shown in the respective two insets.

2.2 Manipulating the atoms

After obtaining a BEC, we can start the interferometric sequence of the SGI, consisting of RF pulses and magnetic gradients. Before that we prepare the atoms in the desired initial position and internal state.

2.2.1 Initial position – changing the trap position

At the end of the evaporation the trap is located $\sim 400 \mu\text{m}$ below the chip surface. To get strong gradients the atoms should be closer to the chip, and preferably be positioned at the center of the quadrupole field for maximum stability (see Sec. 1.5). To achieve this, the trap position is changed by ramping down the current in the Z wire to 24.42 A, and the y -bias field to 41 G, which brings the trap closer to the chip. We simultaneously turn on the current in the z -bias coils to produce a bias field of -2.6 G which optimizes the position of the trap in the y direction. If the atoms are not positioned directly below the center of the chip, there will be a force pushing them in the y direction and the two interferometer arms will separate along the y -axis, which will reduce their final overlap and reduce the visibility of the interferometer fringes. Since we image along the y -axis, we cannot measure the position of the atoms along this axis directly, so optimizing the z -bias field is done by measuring the interference visibility. It is important to change the fields slowly enough so that the position is changed adiabatically, so we ramp the currents during 250 ms to prevent oscillations and heating, and wait another 150 ms so that the cloud will stabilize in the trap.

2.2.2 Initial state – cleaning residual $m_F = 1$

For optimal operation of the SGI, a pure state is required. The final state of atoms in the trap however, is a mixture of atoms in $m_F = 2$ and $m_F = 1$. The latter is due to the RF radiation in the

evaporative cooling stage, in which atoms in the $m_F = 2$ state undergo transitions to untrapped states through $m_F = 1$, thereby leaving around 10% of the atoms in the $m_F = 1$ state. We remove these $m_F = 1$ atoms from the trap by applying an RF field to couple the $m_F = 1$ state to the untrapped $m_F = 0$ state. The applied RF field does not affect the $m_F = 2$ atoms, because it is not resonant with the $m_F = 2 \rightarrow m_F = 1$ transition as discussed next.

2.2.3 Internal state manipulation

Effective two-level system

By applying a strong magnetic field in the y direction we can exploit the non-linear Zeeman effect, and get an effective two-level system. We run 49 A in the y -bias coils, generating a magnetic field of 35.3 G which results in a transition frequency between the $m_F = 2$ and $m_F = 1$ states, $f_{21} \approx 24.7$ MHz. At this field the transition frequency difference is $f_{21} - f_{10} = 180$ kHz so the $m_F = 1 \rightarrow 0$ transition is out of resonance as long as the power broadening is low enough. By applying on-resonance RF radiation we couple the $m_F = 2$ and $m_F = 1$ sub-levels to induce Rabi oscillations and perform different RF sequences to manipulate the internal state.

Rabi oscillations

We apply on-resonance RF pulses to create different coherent superpositions of the two Zeeman sub-levels $|F = 2, m_F = 2\rangle$ and $|F = 2, m_F = 1\rangle$ (which we denote simply as $|2\rangle$ and $|1\rangle$). It is helpful to represent the state of a two-level system on the Bloch sphere, by defining the north pole of the Bloch sphere as the state $|2\rangle$ and the south pole as the state $|1\rangle$ (Fig. 2.5). Any state of the two-level system $|\psi\rangle$ can then be described by two angles, θ and ϕ , so that $|\psi\rangle = \cos(\theta/2)|2\rangle + e^{i\phi} \sin(\theta/2)|1\rangle$. We define a “ π pulse” as a pulse that takes the Bloch vector from the north pole ($\theta = 0$) to the south pole ($\theta = \pi$). Starting from the state $|\psi\rangle = |2\rangle$ and applying a π pulse will result in the state $|\psi\rangle = |1\rangle$. A $\pi/2$ pulse is a pulse that takes the Bloch vector from the north pole to the equator ($\theta = \pi/2$), so starting from the state $|\psi\rangle = |2\rangle$ and applying a $\pi/2$ pulse will result in the state $|\psi\rangle = \frac{1}{\sqrt{2}}(|2\rangle + |1\rangle)$. As a source for the RF pulses we use the SRS-SG384 signal generator, since it has good phase modulation that we use to control the relative phase between the $\pi/2$ pulses. The RF chain is then followed by an RF shutter for quick switching ($\sim 1 \mu\text{s}$ rise time), and a Mini-Circuits RF amplifier. As an antenna we use the copper structure under the chip (Fig. 1.1). The typical duration of a π pulse is $20 \mu\text{s}$, and we calibrate the RF frequency and amplitude to make sure that the pulse is on resonance and that its area is indeed π . The phase of the pulse determines the rotation axis around which the Bloch vector rotates, while the duration (area) of the pulse determines the angle of the rotation (Fig. 2.5).

Ramsey sequence

A Ramsey sequence consists of two $\pi/2$ pulses with a time delay between them. We start with the initial state $|\psi\rangle = |2\rangle$ and apply a $\pi/2$ pulse to get $|\psi\rangle = \frac{1}{\sqrt{2}}(|2\rangle + |1\rangle)$. The frame of reference is rotating with the RF signal, so the relative phase ϕ evolves as $\phi = (\omega_0 - \omega_{\text{RF}}) \cdot T_{\text{Ramsey}} = \delta\omega \cdot T_{\text{Ramsey}}$ where ω_0 is the resonance frequency of the atoms, ω_{RF} is the frequency of the RF radiation, and T_{Ramsey} is the time between the two pulses. The evolution of the state in the rotating frame can be written as $|\psi(t)\rangle = \frac{1}{\sqrt{2}}(|2\rangle + e^{-i\phi}|1\rangle)$. The second $\pi/2$ pulse transfers the system to the state $|\psi(t)\rangle = \frac{1}{2}[(1 - e^{-i\phi})|2\rangle + (1 + e^{-i\phi})|1\rangle]$, and the probability of finding the atoms in the state $|1\rangle$ is

$$P_1 = \frac{1}{2}[1 + \cos(\phi)] = \frac{1}{2}[1 + \cos(\delta\omega \cdot T_{\text{Ramsey}})]. \quad (2.2)$$

As we increase T_{Ramsey} we observe oscillations in the population P_1 , which are named Ramsey fringes. When observing an ensemble of atoms, effects of non-homogeneity will cause a decay of the

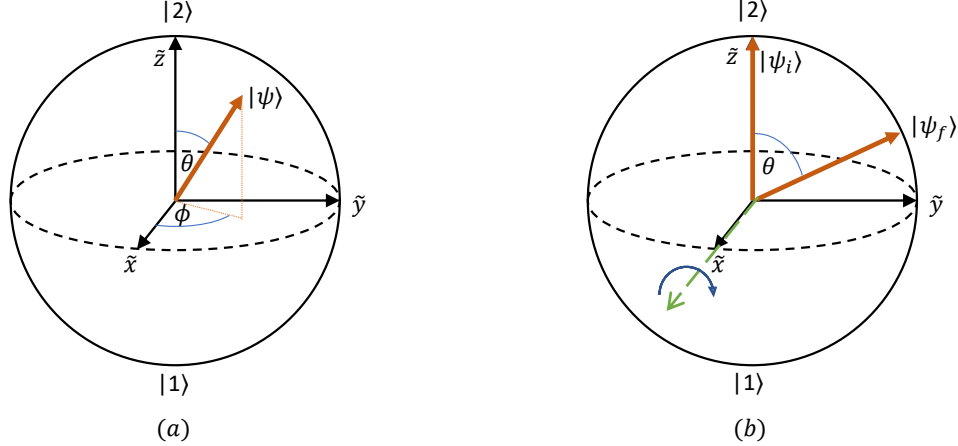


Figure 2.5: Bloch sphere representation of a two-level system: (a) The Bloch sphere with the north pole of the Bloch sphere representing the state $|2\rangle$ and the south pole representing the state $|1\rangle$. The red arrow is the Bloch vector of the state $|\psi\rangle = \cos(\theta/2)|2\rangle + e^{i\phi} \sin(\theta/2)|1\rangle$. (b) Rotation of the Bloch vector around the \tilde{x} -axis at angle θ , from the state $|\psi_i\rangle = |2\rangle$ to the state $|\psi_f\rangle = \cos(\theta/2)|2\rangle + \sin(\theta/2)|1\rangle$. In the $\pi/2$ and π pulses which we use in this work, the latter represent the values of θ . We note that the \tilde{z} axis of the Bloch sphere is defined as the quantization axis, and in our experiment is different from the real space z axis

oscillation amplitude, since each atom has a slightly different resonance frequency, resulting in a different final phase, and as the phase spread increases, the oscillation’s contrast decays. The time constant of the decay is called the coherence time. To increase the coherence time, we may apply a “spin-echo” technique [25]. Another feature of the Ramsey sequence is its sensitivity to the detuning $\delta\omega$. It is clear that if the detuning fluctuates from shot to shot, the phase will fluctuate, and the population will fluctuate non-linearly due to the trigonometric relation. The relation between the phase noise and the population noise is discussed in Appendix A at length. Spin-echo techniques also significantly reduce the shot-to-shot phase noise, and are discussed next.

Spin-echo

The spin-echo technique was developed in nuclear magnetic resonance (NMR) to increase the coherence time of systems and to reverse the effect of inhomogeneous fields. In our system it also helps reduce shot-to-shot phase fluctuations. The sequence consists of two $\pi/2$ pulses with a π pulse in the middle of the two. The π pulse reverses the evolution of the state, so that the phase contribution from the first half $\phi_1 = \delta\omega \cdot T$ cancels the opposite phase in the second half $\phi_2 = -\delta\omega \cdot T$. Assuming that the detuning is the same in both halves, the total phase $\phi_1 + \phi_2$ is zero for any value of $\delta\omega$, thereby reducing effects due to shot-to-shot fluctuations of $\delta\omega$ which may arise from low frequency noise in the bias field. This kind of noise will be discussed in detail in Appendix A.

2.2.4 Population measurement

In most of our experiments we need to measure the relative population in the different Zeeman sub-levels, whether for calibrating the Rabi pulse, or for measuring the relative population in each output port of the SGI. The measurement sequence is simple. We first separate the two states spatially by applying a magnetic gradient in the z -direction. This creates a differential force on the two states due to the magnetic interaction, $F = -\frac{\partial U}{\partial z} = \mu \cdot \frac{\partial B}{\partial z} \approx m_F g_F \mu_B \frac{\partial B}{\partial z}$. The gradient duration is 1 – 3 ms and is produced by running a high current in the copper Z -wire. After a TOF of another few ms, the two states can be spatially resolved by our imaging system and we apply the absorption imaging pulses, as described in Sec. 1.4. The image shows the two clouds, to which

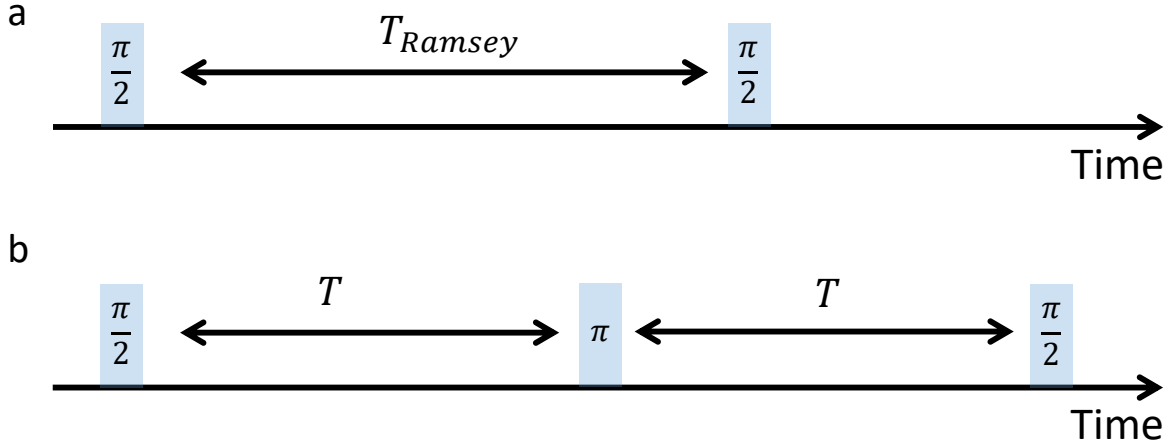


Figure 2.6: Ramsey and spin-echo sequences. (a) Ramsey sequence, consisting of two $\pi/2$ pulses, with a delay time of T_{Ramsey} between them. (b) Spin-echo sequence, consisting of two $\pi/2$ pulses with a π pulse exactly in the middle.

we apply a 2D-Gaussian fit to count the atoms in each cloud and calculate the relative population in each state. To detect clouds having low OD and a small number of atoms, we apply a low-pass filter to the image.

2.2.5 Stern-Gerlach splitting using the atom chip

Magnetic force from a three-wire configuration

To suppress phase noise, which mainly comes from fluctuations in the chip modulated currents and is proportional to the magnitude of the magnetic field produced by the chip wires, we maintain the gradient while minimizing the magnetic field by forming a quadrupole field and placing the atoms close to its zero-field center. The quadrupole field is formed by three parallel current-carrying wires. Let us derive the force applied on the atoms by currents through three infinitely-long parallel wires, which is useful for estimating the actual magnetic gradient forces in the experiment. The three wires are oriented along the x -axis, located at $y = -d, 0, d$ (for our chip $d = 100 \mu\text{m}$, see Fig. 2.7). The currents in the outer wires are directed along $-x$ while the central wire current is along $+x$ while the magnitudes of the currents are the same in all three wire. Due to the fact that the two external wires cancel each other's field in the z direction, the field directly below the central wire ($x = 0$) points in the y direction. An additional strong magnetic bias field B_y^0 is applied. The total magnetic field is

$$\mathbf{B} = (0, B_y, 0), \text{ where } B_y = B_y^0 - \frac{\mu_0 I}{2\pi} \left[\frac{1}{z} - \frac{2z}{z^2 + d^2} \right]. \quad (2.3)$$

Under the adiabatic approximation, the magnetic potential is given by

$$U = -\boldsymbol{\mu} \cdot \mathbf{B} \approx m_F g_F \mu_B |\mathbf{B}|. \quad (2.4)$$

The force on the atoms in state m_F is given by

$$\begin{aligned} F_B &= -\nabla U = -\nabla(-\boldsymbol{\mu} \cdot \mathbf{B}) \approx -\nabla(m_F g_F \mu_B |\mathbf{B}|) = -m_F g_F \mu_B \nabla |\mathbf{B}| \\ &= -m_F g_F \mu_B \left(\frac{\partial}{\partial x}, \frac{\partial}{\partial y}, \frac{\partial}{\partial z} \right) \sqrt{(B_y)^2} \\ &= -m_F g_F \mu_B \frac{\mu_0 I}{2\pi} \left[\frac{1}{z^2} + 2 \frac{d^2 - z^2}{(d^2 + z^2)^2} \right] \text{sign}[B_y(z)] \hat{z}. \end{aligned} \quad (2.5)$$

This expression assumes the atoms are exactly below the chip center and in this situation the force is exerted only in the z direction. The force calculated at $z = d$ gives the same result as the single wire configuration because the second term in the brackets zeros out when $z = d$, leaving only the contribution due to the central wire. The direction of the force may be reversed experimentally by reversing the direction of the currents. Eq. 2.5 is not exact as the wires have finite length and finite width; the fields generated by the chip wires are numerically calculated when necessary using the chip wire parameters.

2.3 Troubleshooting a complex experimental procedure

The experimental apparatus that we were lucky to inherit from our predecessors is a complex and sensitive 12 year old machine, with hundreds of components, and hundreds of analog and digital signals each cycle. We have lots of home-made components ranging from mechanical light shutters, to AOM drivers, and a laser (which is actually very reliable). Problems are bound to happen and devices are bound to malfunction. The phase transition to a BEC is very sensitive and every small change in the experimental parameters can prevent achieving a BEC. Small changes in laser frequency (1-2 MHz), intensity or polarization of the beams during the MOT stage or the preparation for the magnetic trap, lead to unoptimized trapping and cooling. Changes of less than 0.1% in the bias fields during the evaporative cooling will change the trap bottom and prevent getting a BEC, and the same may be said for small changes in timing of triggers and ramps. With such a sensitive system, one main concern is to keep it working well, and the usual good morning greetings are answered with “we have a BEC / we don’t have a BEC”. When facing a problem, you initially have no clue if it is a matter of routine calibrations, like laser intensities and fine tuning of the RF ramps, or a malfunction like a burnt current shutter, or just a wrong number you entered for one of the cycle stages. Troubleshooting such a complex experimental procedure (sequence) becomes an art, and to finalize this chapter, I would like to briefly list some of the maintenance tasks I had to perform as part of this M.Sc. work:

1. Documentation - Everything you do has to be written down. Even one line can save you tons of work. You will forget in two weeks that you changed the channel of some event, connected a new component, or easily fixed a problem which may come back. As an example, optimization and calibration of the MOT and trap loading, that originally took more than a week, was repeated in less than a day, because only the parameters that showed significant effects the first time required optimization the second time.
2. Routine calibrations - Every system needs check-lists. Here I detail the main items we had on our regular check-list: We re-couple the laser to the fibers every week or two, or if the fluorescence signal of the MOT is smaller than usual. We calibrate the RF ramps once in awhile or if the number of atoms in the BEC is not optimal; usually calibrating the last ramp or two is enough. We calibrate the resonance frequency and amplitude of the Rabi pulses before every data-taking session. We optimize the coupling of the laser diode to the TA if the output intensity is not high enough. We adjust the magnetic fields to get optimal loading to the trap.
3. Inherent problems - Some problems tend to repeat themselves. Usually these problems are easy to solve, but hard to diagnose. In our system repeating malfunctions are: current shutters burn routinely and need replacement, light leakage that kills the BEC happens often as there are numerous potential sources for such a leak, and finally, the laser can drift from single-mode operation.
4. Diagnosing malfunctions and problem solving - We diagnosed and solved many problems during this work, such as electrical noise from a faulty lamp in the lab that “killed” the BEC, optimizing the MOT beam alignment and polarization after replacing the main laser, diagnosing degradation of the dispensers and installing UV LEDs to compensate for this,

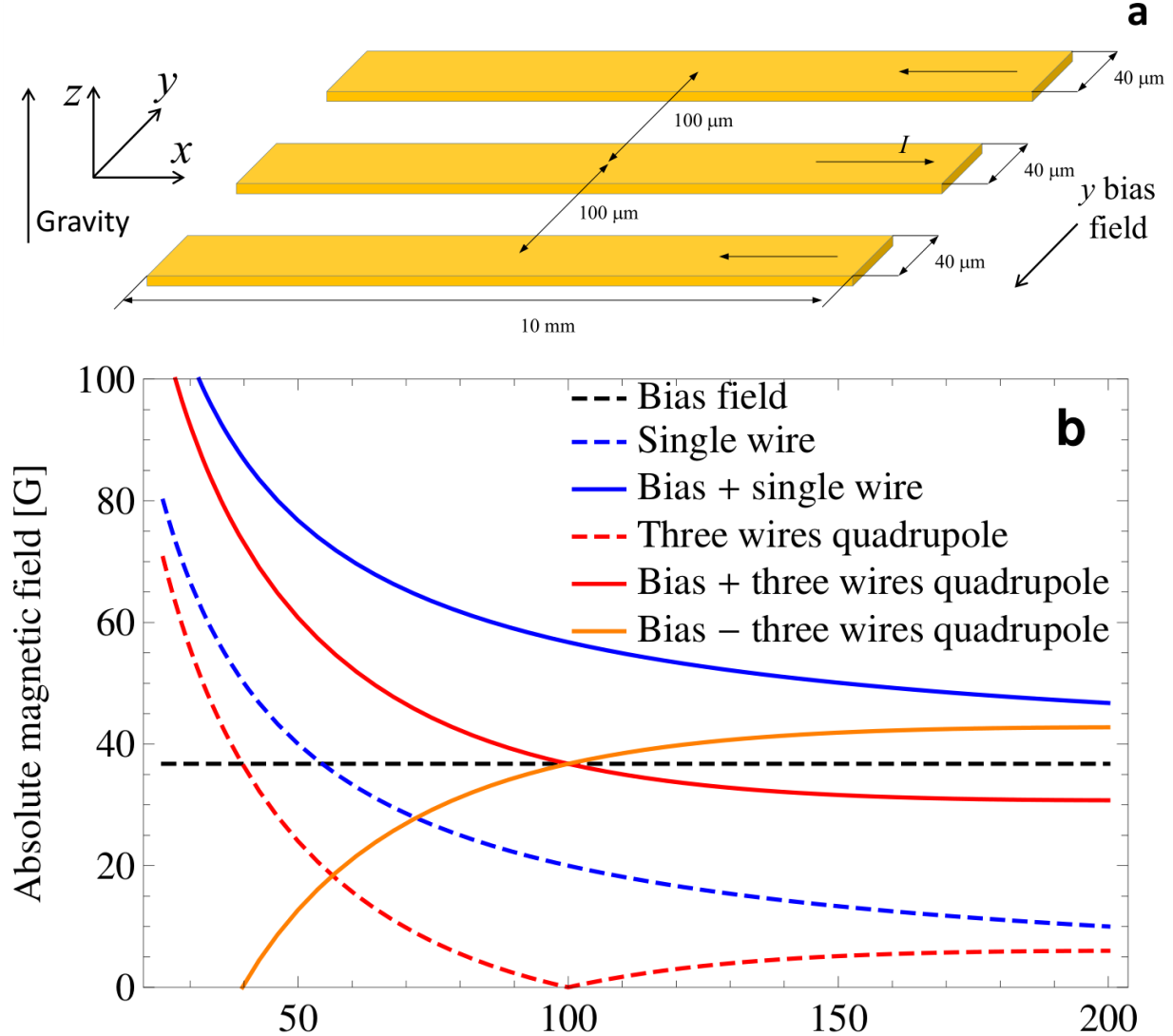


Figure 2.7: Quadrupole field of the atom chip and its advantages. (a) Schematic diagram of the chip wires which are used to generate the quadrupole field. Wires are 10 mm long, $40\ \mu\text{m}$ wide and $2\ \mu\text{m}$ thick. The separation between the wires' centers is $100\ \mu\text{m}$, and the direction of the current I alternates from one wire to the next. The wires, being much smaller than the size of the chip ($25\ \text{mm} \times 30\ \text{mm}$), are hardly visible in Fig. 1.2. (b) While the constant-bias magnetic field (dashed black line) is necessary to create an effective two-level system, we do not require any additional bias to be produced by the chip wires during the gradient pulses, but require only the gradient of the field. This requires only a single wire. However, one can see that the total magnitude of the magnetic field produced by a quadrupole and a bias (red/orange lines) is smaller than that produced by a single wire and a bias (blue line, as used in [5]), while the gradient (at $100\ \mu\text{m}$) is the same. Since the phase noise is largely proportional to the magnitude of the magnetic field created during the splitting pulse [5], positioning the atoms near the quadrupole position ($98\ \mu\text{m}$ below the chip surface) reduces the phase noise. Taken from [13].

and many other malfunctions. One hard-to-diagnose problem was a malfunction in the x -bias power supply chain; a small increase in the resistance of the current shutter limited the maximal current output of the power supply, from $\sim 51\ \text{A}$ to $48.2\ \text{A}$ at the maximum voltage of the power supply which is $6\ \text{V}$. This change of the x -bias field affected the trap bottom and thus most of the atoms were expelled from the magnetic trap during the evaporative cooling. The loss of atoms was thought to be due to different reasons mainly that the atoms

were not cold enough before loading them into the magnetic trap due to suboptimal cooling during the molasses. It was finally diagnosed by imaging the atoms at different times during the evaporative cooling that showed a sharp loss of atoms 2s into the evaporative cooling stage in less than 0.1 s. The sudden loss of atoms indicated that the trap bottom has changed which led us to suspect the magnetic fields during this stage were changed. We replaced the power supply and carefully calibrated the current in the new power supply with a $6\frac{1}{2}$ -digit multimeter, so that it will give the same current as the old one up to a 0.1% error margin, as we found this precision is necessary if one wishes to avoid re-tuning all the RF ramps. After we calibrated currents we fine-tuned the two last RF ramps to get an optimal BEC. The problem was harder to diagnose as the malfunction began sometime during the down-time period of replacing the main laser and realigning the MOT beams. At this point we didn't suspect a new problem will arise during the evaporative cooling stage, as this stage was not changed or affected by the replacement of the laser or the alignment of the MOT beams. Of course, such a malfunction can appear so it is important to keep the down time of the experiment to a minimum when replacing a component. We applied this lesson to the replacement of the laser diode in the TA-100; we first stabilized the experimental sequence in its new state after the replacement of the laser, alignment of the MOT beams, and replacement of the x -bias power supply. Once the experiment was stable the problem of multi-mode operation could be isolated and we went on to replace the laser diode which indeed solved this problem.

Chapter 3

Atom Interferometry

3.1 Interferometry in the history of physics

Interferometers have long been a crucial part in our investigation of nature and physical phenomena. Particularly famous interferometer experiments range from Young’s double slit experiment that explored the wave-like nature of light to the Michelson-Morley experiment, with its brave attempt to measure the Earth’s movement in the “luminiferous aether”. The Michelson-Morley experiment was one of the experimental foundations of special relativity. Its ultimate extension in the modern era is the Laser Interferometer Gravitational-Wave Observatory (LIGO), an example of a large-scale experiment built with the goal of detecting gravitational waves and that successfully confirmed Einstein’s predictions 100 years after the theory of general relativity. The leap from optical interference to matter-wave interference was made around 1924, with the de Broglie hypothesis confirmed by the Davisson-Germer experiment that demonstrated the wave properties of electrons, exhibiting a diffraction pattern, similar to X-ray scattering experiments. Atom interferometers were first developed in the 1990’s, and nowadays are common devices for research in the field of quantum mechanics and are used in precision measurements of gravity [2], fundamental constants [3], and as accelerometers for inertial guidance and many additional endeavors [4]. A detailed review of atom interferometry may be found in [1].

In the following chapters we present our work on the Stern-Gerlach atom interferometer, in which the splitting and recombination of quantum wavepackets is performed by forces that arise from magnetic gradients acting on Zeeman sub-levels. Our atom interferometer is realized on the atom chip, and stands at the opposite end of scale of the LIGO facility. Nevertheless, it is hoped that it too has unique properties that will enable new insights in fundamental science as well as technological applications.

3.2 Stern-Gerlach Interferometer (SGI)

In 1922 Walther Gerlach and Otto Stern published their results on “The experimental proof of directional quantization in the magnetic field”, which is now famously known as the Stern-Gerlach (SG) experiment [26]. In the experiment, a collimated beam of silver atoms passed through a region with a strong magnetic gradient. The results showed a splitting into two distinct beams and were clear evidence of the quantization of the magnetic dipole of the atom. The SG experiment contributed to the discovery of quantum mechanical spin, the intrinsic angular momentum of particles. While the SG experiment demonstrated splitting of an atomic beam into two distinct beams, it did not demonstrate the coherence of the splitting process; to prove coherent superposition one has to show an interference signal. The spatial fringe SGI, showing a spatial interference pattern, and the full-loop SGI, showing spin population fringes, will be described in the next subsections,

and prove the coherence of splitting and recombination of wavepackets via the application of magnetic gradients. Finally, let us comment on the previous world state-of-the-art in SG interferometry with static magnetic fields [27–37]. While these longitudinal beam experiments did observe spin-population interference fringes, the experiments presented here are very different. Most importantly, as explained in [32] and [35], the full-loop configuration was never realized, since only splitting and stopping operations were applied (i.e., there was no active recombination); namely, wavepackets exit the interferometer with the same separation as the maximal separation achieved within.

3.2.1 Half loop – spatial fringes

In 2013, our laboratory’s team demonstrated coherent Stern-Gerlach splitting [5, 11] of an atomic wavepacket, establishing the Stern-Gerlach beam splitter (SGBS), and showing for the first time a spatial interference patterns from an SG apparatus (the SGBS was originally coined the field-gradient beam splitter FGBS). The experiment is an atomic analog of the double slit experiment, first splitting the wavepackets, then stopping their acquired momentum after some propagation time, and finally allowing them to expand until they overlap and exhibit a spatial interference pattern. A detailed analysis of the stability of the Stern-Gerlach spatial fringe interferometer was recently published [7], demonstrating the very high phase stability of our implementation, in which the multi-shot fringe visibility reached 90%. The spatial fringe SGI technique was used for further experiments in our laboratory, where the two wavepackets were put in a clock state and the different “ticking” rates, induced by a synthetic red-shift of proper time, gave rise to “which path” information that affected the fringe visibility [38]. An experiment with a similar setup showed the quantum complementarity of clocks [39], extending the known quantum complementarity relation for visibility and distinguishability $V^2 + D^2 \leq 1$ [40] where V is interference pattern visibility and D is the distinguishability of the two paths of the interfering particle. In an experiment where the proper time is a “which path” witness, the clock complementarity relation becomes $V^2 + (C \cdot D_I)^2 \leq 1$ where D_I is the ideal clock distinguishability of the paths, determined by the different ticking rate in the two paths of the clock, and $0 \leq C \leq 1$ is the clock quality, whereby D_I is due to the red-shift of general relativity, and C is due to the quantum preparation of the two-level clock. The maturity of these and other [41] half-loop SGI experiments in our laboratory has paved the way for exploring the full-loop SGI, which is described in this thesis.

The experimental signal in the half loop is a spatial interference fringe pattern, containing information about the visibility, periodicity and phase of the interferometer. The spatial fringe is produced by the interference of two wavepackets having the same spin. To produce high visibility spatial fringes, it is not necessary to actively recombine the paths of the wavepackets, and the stopping of the relative motion doesn’t have to be precise. As long as the momentum distribution of each of the wavepackets is wider than the momentum difference after stopping, the wavepackets’ expansion guarantees that they will eventually overlap and the visibility will be high. It is even possible to increase the momentum distribution by a lensing effect of the gradients which makes the wavepackets expand more rapidly. It follows that the half-loop interferometer does not require high precision of the splitting and stopping operations but rather requires high repeatability of these operations from shot to shot, which is essential for high phase stability.

In contrast, the full-loop SGI, based on splitting and recombination of two wavepackets with different spin states, does require precision in the recombination of the wavepackets, as discussed in the next sections.

3.2.2 Full loop SGI – spin population fringes

In 1951 David Bohm envisioned an atom interferometer based on the SG experiment, using permanent magnets to create four regions of magnetic gradients to split, stop, reverse, and recombine the wavepackets in a setup analogous to a Mach-Zehnder (MZ) interferometer. Bohm mentioned

that such a device would require “fantastic” accuracy [42]. Englert, Schwinger and Scully analyzed the concept of an SGI in more detail and coined it the “Humpty-Dumpty” (HD) effect [8–10] to emphasize that exceptional precision would be required to coherently split and recombine the wavepackets.

In our realization, the full-loop SGI is based on a sequence of RF pulses to manipulate the internal state of the atoms, i.e., a two-level system of Zeeman sub-levels $|1\rangle$ and $|2\rangle$, and pulses of magnetic gradients originating from an atom chip to manipulate the external degrees of freedom of the atoms. We apply four magnetic gradient pulses to split, stop, reverse, and recombine the wavepackets in momentum and position. The detailed experimental sequence will be presented in Sec. 4.1. We start with the atoms in state $|2\rangle$, then apply the first $\pi/2$ RF pulse which creates an equal spin superposition $|\psi\rangle = \psi_0(\mathbf{r})\frac{1}{\sqrt{2}}(|1\rangle + |2\rangle)$, where $\psi_0(\mathbf{r})$ is the initial wavepacket. We then apply the gradient pulses to manipulate the momentum and position of the wavepackets. The wavefunction throughout the propagation in the interferometer is a superposition with two different spatial wavepackets evolving separately along the interferometer arms

$$|\psi(\mathbf{r}, t)\rangle = \frac{1}{\sqrt{2}}[\psi_1(\mathbf{r}, t)|1\rangle + \psi_2(\mathbf{r}, t)|2\rangle]. \quad (3.1)$$

After the last gradient pulse we apply the second $\pi/2$ RF pulse and finally measure the population in the $|1\rangle$ state as described in Sec. 2.2.4. The state after the last gradient pulse is $|\psi(\mathbf{r}, t_f)\rangle = \frac{1}{\sqrt{2}}[\psi_1(\mathbf{r}, t_f)|1\rangle + \psi_2(\mathbf{r}, t_f)|2\rangle]$, and after applying the second (and last) $\pi/2$ RF pulse we get

$$|\psi(\mathbf{r}, t_f)\rangle = \frac{1}{2}[\psi_1(\mathbf{r}, t_f)(|1\rangle - |2\rangle) + \psi_2(\mathbf{r}, t_f)(|1\rangle + |2\rangle)]. \quad (3.2)$$

The measurement of population is a projection into state $|1\rangle$, where after the projection we get

$$\langle 1|\psi(\mathbf{r}, t_f)\rangle = \frac{1}{2}[\psi_1(\mathbf{r}, t_f) + \psi_2(\mathbf{r}, t_f)] \quad (3.3)$$

and the measured population, i.e., the fraction of atoms in the $|1\rangle$ state, is

$$P_1 = \int d^3\mathbf{r} |\langle 1|\psi(\mathbf{r}, t_f)\rangle|^2 = \frac{1}{4} \int d^3\mathbf{r} (|\psi_1|^2 + |\psi_2|^2 + \psi_1^*\psi_2 + \psi_1\psi_2^*). \quad (3.4)$$

Since the wavefunctions ψ_1 and ψ_2 are normalized, $\int d^3\mathbf{r} |\psi_1|^2 = \int d^3\mathbf{r} |\psi_2|^2 = 1$, we obtain $P_1 = \frac{1}{4}[2 + \int d^3\mathbf{r} (\psi_1^*\psi_2 + \psi_1\psi_2^*)]$, which gives

$$P_1 = \frac{1}{2} [1 + V \cos(\Delta\phi)], \quad (3.5)$$

where

$$Ve^{-i\Delta\phi} = \int d^3\mathbf{r} \psi_1^*(\mathbf{r}, t_f)\psi_2(\mathbf{r}, t_f) \quad (3.6)$$

is the overlap integral. Here V is the spin population fringe visibility and $\Delta\phi$ is the interferometric phase. The different contributions to this phase and the visibility are described in the next two sections.

3.3 Phase of the SGI

Here we explain and calculate the interferometer phase $\Delta\phi$ in Eq. 3.6, which is the phase difference between the two wavepackets ψ_1 and ψ_2 , acquired during the propagation in the two arms. The centers of the two wavepackets follow two trajectories $\mathbf{R}_1(t)$ and $\mathbf{R}_2(t)$ along the two interferometer arms such that at the final time t_f they are located at the points $\mathbf{R}_1(t_f)$ and $\mathbf{R}_2(t_f)$ and have corresponding momenta $\mathbf{P}_1(t_f)$ and $\mathbf{P}_2(t_f)$. We can write two wavefunctions ψ_1 and ψ_2 in the form

$$\psi_j(\mathbf{r}, t_f) = e^{i\mathbf{P}_j \cdot (\mathbf{r} - \mathbf{R}_j)/\hbar} \Phi_j(\mathbf{r} - \mathbf{R}_j, t_f) e^{iS_j/\hbar}, \quad (3.7)$$

where (for $j = 1, 2$) \mathbf{R}_j and \mathbf{P}_j are the positions and momenta at the final time t_f (the argument t_f is omitted for brevity), S_j are the corresponding actions along the two classical trajectories, and $\Phi_j(\mathbf{r}, t_f)$ is the wavefunction in the frame of reference that moves with $\mathbf{R}_j(t)$ of each arm, which we assume to be the same for both arms [meaning $\Phi_1(\mathbf{r}, t_f) = \Phi_2(\mathbf{r}, t_f)$]. This assumption is fully justified if the time evolution involves only homogeneous gradients since such gradients affect only the momentum of the wavepackets. In our realization the gradients are not completely homogeneous but the deviation from this assumption due to the differential curvature of the gradients is negligible. We note that we allow a time delay between the last gradient and the last $\pi/2$ RF pulse, during which the wavepackets are assumed to be exposed to the same unitary time evolution which conserves the overlap integral in Eq. 3.6, i.e., the visibility and the phase.

We define $\mathbf{R}_{\text{avg}} = \frac{1}{2}[(\mathbf{R}_1(t_f) + \mathbf{R}_2(t_f))]$ and $\delta\mathbf{R} = \mathbf{R}_1 - \mathbf{R}_2$, to get $\mathbf{R}_j = \mathbf{R}_{\text{avg}} \pm \frac{1}{2}\delta\mathbf{R}$, where $+$ and $-$ refer to $j = 1, 2$, respectively. In the same manner we define $\mathbf{P}_{\text{avg}} = \frac{1}{2}(\mathbf{P}_1 + \mathbf{P}_2)$ and $\delta\mathbf{P} = \mathbf{P}_1 - \mathbf{P}_2$, to get $\mathbf{P}_j = \mathbf{P}_{\text{avg}} \pm \frac{1}{2}\delta\mathbf{P}$. Using this we write the phase in the first exponent

$$\frac{1}{\hbar}\mathbf{P}_j \cdot (\mathbf{r} - \mathbf{R}_j) = \frac{1}{\hbar}(\mathbf{P}_{\text{avg}} \pm \frac{1}{2}\delta\mathbf{P}) \cdot (\mathbf{r} - \mathbf{R}_{\text{avg}} \mp \frac{1}{2}\delta\mathbf{R}). \quad (3.8)$$

By substituting the wavefunctions in Eq. (3.7) into the overlap integral in Eq. (3.6) we obtain

$$V e^{-i\Delta\phi} = e^{-\frac{i}{\hbar}[\Delta S - \mathbf{P}_{\text{avg}} \cdot \delta\mathbf{R}]} \int d^3\mathbf{r} e^{-i\delta\mathbf{P} \cdot (\mathbf{r} - \mathbf{R}_{\text{avg}})} \Phi^*(\mathbf{r} - \mathbf{R}_{\text{avg}} - \frac{1}{2}\delta\mathbf{R}, t_f) \Phi(\mathbf{r} - \mathbf{R}_{\text{avg}} + \frac{1}{2}\delta\mathbf{R}, t_f). \quad (3.9)$$

We now transform the integration variable to $\mathbf{r}' = \mathbf{r} - \mathbf{R}_{\text{avg}}$

$$V e^{-i\Delta\phi} = e^{-\frac{i}{\hbar}[\Delta S - \mathbf{P}_{\text{avg}} \cdot \delta\mathbf{R}]} \int d^3\mathbf{r}' e^{-i\delta\mathbf{P} \cdot \mathbf{r}'} \Phi^*(\mathbf{r}' - \frac{1}{2}\delta\mathbf{R}, t_f) \Phi(\mathbf{r}' + \frac{1}{2}\delta\mathbf{R}, t_f). \quad (3.10)$$

Note that the integral in Eq. (3.10) is real if the wavefunction $\Phi(\mathbf{r}, t_f)$ is symmetric or antisymmetric under inversion, because taking the complex conjugate of the integrand gives the same integrand with reversed coordinates $\mathbf{r} \rightarrow -\mathbf{r}$. It follows that the integral can be identified with the visibility V , while the phase can be identified with

$$\Delta\phi = \frac{1}{\hbar}\Delta S - \frac{1}{\hbar}\mathbf{P}_{\text{avg}} \cdot \delta\mathbf{R} = \frac{1}{\hbar}\Delta S - \Delta\varphi_{\text{sep}}, \quad (3.11)$$

where $\Delta S = S_1 - S_2$ is the action difference between the two centers of the wavepackets, $\delta\mathbf{R}$ is the spatial separation at time t_f , and $-\frac{1}{\hbar}\mathbf{P}_{\text{avg}} \cdot \delta\mathbf{R} \equiv \Delta\varphi_{\text{sep}}$ is the separation phase which appears if the two arms have some final spatial separation, and which depends on the average momentum of the two arms \mathbf{P}_{avg} . The decomposition of the phase in this way is not unique and depends on the frame of reference in which the calculation is done; for example, in a frame of reference that moves with the average velocity of the final wavepackets, the separation phase would vanish for any $\delta\mathbf{R}$, as $\mathbf{P}_{\text{avg}} = 0$. We now examine more closely these two contributions to the phase: the action difference and the separation phase.

3.3.1 The action difference

The action of each arm is the integral over the classical path $S_j = \int_0^{t_f} [K_j(t) - U_j(t)] dt$, where $K_j(t)$ and $U_j(t)$ are the kinetic and potential energies, respectively, so the action difference is

$$\frac{1}{\hbar}\Delta S \equiv \Delta\varphi_{\text{prop}} = \frac{1}{\hbar} \int_0^{t_f} [\Delta K(t) - \Delta U(t)] dt, \quad (3.12)$$

where $\Delta K(t)$ and $\Delta U(t)$ are the kinetic and potential energy differences between the two arms at any time t during the interferometric sequence. Our interferometer is one dimensional (motion along \hat{z}) so the potential energy difference is

$$\Delta U(t) = -mg[z_1(t) - z_2(t)] - m[a_{B1}(t)z_1(t) - a_{B2}(t)z_2(t)], \quad (3.13)$$

where m is the mass, $a_{B1}(t), a_{B2}(t)$ are the accelerations due to the magnetic gradients in each of the arms as a function of time, and the gravitational acceleration g is assumed to be along the positive direction of the z -axis. The kinetic energy difference is

$$\Delta K(t) = \frac{1}{2}m[v_1^2(t) - v_2^2(t)], \quad (3.14)$$

where $v_1(t), v_2(t)$ are the velocities in each of the arms as a function of time.

Our full-loop SGI is a closed interferometer, where the last two gradient pulses (reversing and recombining) completely undo the action of the two first pulses (splitting and stopping), so that the final position and momentum of the wavepackets in the two arms are equal (we define a closed interferometer as an interferometer where the final separation in position and momentum, $\delta\mathbf{R}(t_f)$ and $\delta\mathbf{P}(t_f)$, are zero.) The sequence consists of four gradient pulses of duration T_1 , where the accelerations $a_{B1}(t), a_{B2}(t)$ are a_1, a_2 during the first and last pulses and $-a_1, -a_2$ during the two middle pulses respectively. There is a delay time T_d between the two first pulses and between the two last pulses (there is no delay between the second and third pulse), during which $a_{B1}(t) = a_{B2}(t) = 0$ (see Fig. 4.1). The interferometric phase of this sequence is calculated from the action difference to be [43]

$$\Delta\phi_{\text{closed}} = \frac{m\Delta a}{\hbar} \left[g(2T_1^3 + 3T_1^2T_d + T_1T_d^2) + (a_1 + a_2) \left(\frac{2}{3}T_1^2 + T_1T_d \right) \right], \quad (3.15)$$

where $\Delta a = a_1 - a_2$ is the acceleration difference.

In this derivation we didn't include the phase due to the interaction with the magnetic bias field. In the frame rotating with the RF frequency (see Sec. 2.2.3), this phase is given by

$$\Delta\phi_B = \int \left(\frac{1}{\hbar} \Delta |\boldsymbol{\mu} \cdot \mathbf{B}_0| - \omega_{\text{RF}} \right) dt, \quad (3.16)$$

integrated over the time delay between the first and last $\pi/2$ RF pulses. In our realization we keep this phase constant and refer to it as φ_0 , since the magnetic bias field and the time delay between the first and last $\pi/2$ RF pulses are constant.

3.3.2 Separation phase of an open SGI

As seen in Eq. 3.11, the interferometer phase contains a term that does not follow from the action difference and appears only in an open geometry where the two arms of the interferometer do not terminate at the same position at $t = t_f$. However, suppose that we wish to measure only the separation phase, in the lab frame. This cannot be done in one measurement. Nevertheless, subtracting the results of two experiments can provide a measurement of the separation phase in an open interferometer that consists of half the sequence of a full-loop closed interferometer. The phase of such an open interferometer (spin population fringes) can be measured if the separation between the two paths is small enough such that the two wavepackets propagating along the two arms still overlap. In our case the closed interferometer sequence is symmetric under inversion around its middle, as the third and fourth pulses are equal to the second and first, respectively. In addition, the second pulse reverses the action of the first momentum kick such that in the middle of the full interferometer the total momentum applied by the pulses is zero. Under these conditions, it can be shown (see Eq. 16 of [44]) that the action difference in the middle of the interferometer is half of the action difference at the end of the full interferometer. We denote by T the time of the half-interferometer ($T = 2T_1 + T_d$), after which $\Delta z = \Delta z_{\text{max}}$ is maximal and $\Delta v = 0$, and by $2T$ the time of the full interferometer, after which $\Delta z(2T) = 0$. Then the action difference satisfies $\Delta S(T) = \frac{1}{2}\Delta S(2T)$. Using this condition and Eq. 3.11, we obtain

$$\Delta\phi(T) - \frac{1}{2}\Delta\phi(2T) = -\frac{1}{\hbar}P_{\text{avg}}\Delta z(T) = \Delta\varphi_{\text{sep}}(T), \quad (3.17)$$

so that measuring the phase at time T and $2T$ enables us to isolate the separation phase from other phase contributions. We note that φ_0 in this open SGI configuration is the same as φ_0 in the closed configuration described above, since the bias field and the timing of the two $\pi/2$ pulses are the same for both configurations. For our realization, the separation phase is calculated to be

$$\Delta\varphi_{\text{sep}} = \frac{mg\Delta a}{\hbar}(2T_1 + T_d + T_0)(T_1T_d + T_1^2), \quad (3.18)$$

where T_0 is the free-fall time from the trap release to the first gradient pulse. In the lab frame, the total phase of an open SGI interferometer will be given by

$$\Delta\phi_{\text{open}} = \frac{1}{2}\Delta\phi_{\text{closed}} + \Delta\varphi_{\text{sep}}. \quad (3.19)$$

3.4 Visibility of the full-loop SGI

3.4.1 Experimental measurement of visibility

We have two methods to experimentally measure the visibility of the SGI. First, we can scan the phase of the second $\pi/2$ RF pulse and fit the resulting pattern to Eq. 3.5, $P_1 = \frac{1}{2}[1 + V \cos(\Delta\phi)]$; this is demonstrated in Fig. S7 of [6]. The second way is by scanning one of the SGI parameters, e.g., maximal momentum splitting or maximal spatial splitting. This is achieved by scanning the gradient pulse duration or delay time between the pulses. In such measurements, both the interferometer phase $\Delta\phi$ and visibility V can change. Fitting the visibility to a function of the gradient pulse duration or delay time determines the visibility for a given set of parameters. In some measurements we observe a decaying oscillation, where V is an envelope decaying as a Gaussian, as explained below.

3.4.2 Theoretical prediction of the visibility

The theoretical prediction of the visibility is based on the estimation of the absolute value of the overlap integral in Eq. 3.6 at the time of measurement. In general, assuming that the atoms are in a BEC state, i.e., all have the same wavefunction in the initial trap, three steps are required to make such a prediction:

1. Writing the initial conditions of the wavepacket – its shape, momentum width, number of atoms, position, etc.
2. Calculating the evolution of the wavepacket, including atom-atom interactions and external potentials.
3. Calculating the overlap integral of the two interferometer arms at the time of measurement.

Under most experimental circumstances, it is hardly ever practical to achieve an exact calculation of the visibility. First, the initial conditions need to be measured, but these have unavoidable experimental uncertainties. Second, to calculate the evolution of the wavepacket, some approximations must be made, since it is impossible to directly calculate the dynamics and interactions of all the atoms. The third step can be done more accurately once we have the final state of the two interferometer arms, since calculating the overlap integral can be done analytically or numerically. A detailed theoretical analysis for the visibility of an SGI with a single atom in a Gaussian wavepacket was conducted by Englert, Schwinger and Scully (ESS) [8–10]. Calculating the overlap integral for two non-expanding Gaussian wavepackets, one gets the HD formula

$$V = \exp \left[-\frac{1}{2} \left(\frac{\sigma_p \Delta z}{\hbar} \right)^2 - \frac{1}{2} \left(\frac{\sigma_z \Delta p_z}{\hbar} \right)^2 \right], \quad (3.20)$$

where σ_p and σ_z are the momentum and spatial widths of the wavepacket, and Δz and Δp_z are the spatial and momentum differences at the moment of measurement. This calculation exhibits a

Gaussian decay of the visibility for increasing spatial or momentum differences. The ESS analysis is an over-simplification for our experiments, in that it shows the general behavior of the visibility, but ignores the time evolution of the wavepackets and the atom-atom interactions in the BEC that also affect the evolution of the wavepacket and therefore the resulting visibility. A better approximation of the initial wavepacket, the wavepacket evolution, atom-atom interactions, and the resulting visibility is presented in [45], and in the next section.

3.4.3 Generalized wavepacket model

The following summary is based on the theoretical development presented by my colleague Yonathan Japha in [45]. Here I summarize the main results related to the full-loop SGI from his work. Another analysis of this problem, with a representation-free form, is presented in [46].

Initial condition – “Generalized Thomas-Fermi approximation”

To get an approximation to the initial wavepacket in our experiment we begin with the Gross-Pitaevskii equation (GPE) for a BEC in a harmonic potential [24]:

$$\left[-\frac{\hbar^2 \nabla^2}{2m} + \frac{m}{2} \sum_{j=1}^3 \omega_j^2 r_j^2 + gN |\Phi_0|^2 - \mu \right] \Phi_0(\mathbf{r}) = 0, \quad (3.21)$$

where the first term is the kinetic energy, the second term is the potential energy in a harmonic trap with frequencies ω_j in the three Cartesian co-ordinates j , and the third term is the mean-field repulsive potential. This term is proportional to the atom density $N |\Phi_0|^2$, where the wavefunction Φ_0 is normalized to unity, and to the coupling strength $g = 4\pi\hbar^2 a_s/m$ with a_s being the s -wave scattering length, m the atomic mass, and μ the chemical potential.

The GPE has two familiar limits, one limit regards neglecting the kinetic energy term, and assuming Φ_0 is in the form of Thomas-Fermi (TF) approximation (an inverted parabola). The other limit assumes the atom-atom interactions are negligible, which leads to a Gaussian wavepacket solution. Instead of using one of this limits, we estimate the kinetic energy by assuming that the wavefunction Φ_0 is an implicit hybridization of a Gaussian and an inverted parabolic wavefunction. We use the Gaussian wavepacket $\Phi_G \propto \exp\left(-\sum_j r_j^2/4\sigma_j^2\right)$ to calculate the kinetic energy in Eq. 3.21, namely

$$-\frac{\hbar^2}{2m} \nabla^2 \Phi_0 \approx \sum_j \frac{\hbar^2}{4m\sigma_j^2} \left(1 - \frac{1}{2} \frac{r_j^2}{\sigma_j^2}\right) \Phi_0, \quad (3.22)$$

and the inverted parabolic wavefunction $\Phi_{TF} \propto \sqrt{1 - \sum_j r_j^2/r_{j,\max}^2}$ that is nonzero only when the argument of the square root is positive, to calculate the interaction term $gN |\Phi_0|^2$. The procedure described here provides fairly good agreement with the numerical solutions of the GPE (see [45] Fig. 1 for details). This approach generalizes the TF approximation to the whole range of atom-atom interaction strengths, from non-interacting atoms (low densities) to the standard TF limit (high atomic densities).

Wavepacket evolution

The wavefunction of the BEC after release from the trap satisfies the time-dependent GPE

$$i\hbar \frac{\partial \psi}{\partial t} = \hat{H}_{MF}(t, \psi) \psi, \quad (3.23)$$

where $\hat{H}_{MF}(t, \psi) = -\frac{\hbar^2}{2m} \nabla^2 + U(\mathbf{r}, t) + g\eta(t)N|\psi|^2$ is the Hamiltonian in the mean-field approximation, $U(\mathbf{r}, t)$ is a time-dependent potential arising from gravity, magnetic gradients, etc., and $\eta(t)N$

is the number of atoms in the wavepacket at any time. The atom number $\eta(t)N$ can change in time in different interferometric situations. For example, if a wavepacket is split equally, then each has $N/2$ particles after achieving sufficient spatial separation, and hence the strength of the mean-field potential decreases for each wavepacket by a factor $\eta = 1/2$. The wavefunction can be written as

$$\psi(\mathbf{r}, t) = e^{i[\mathbf{P} \cdot (\mathbf{r} - \mathbf{R}) + S(t)]/\hbar} \Phi(\mathbf{r} - \mathbf{R}, t), \quad (3.24)$$

where \mathbf{R} and \mathbf{P} are as defined in the beginning of Sec. 3.3. The evolution of the center-of-mass (COM) can be found by using Newton's equations, while the evolution of the wavefunction within the COM frame can be found from the following equation:

$$\Phi(\mathbf{r}, t) = \frac{\exp\left[i\left(\frac{1}{2}\sum_j \alpha_j r_j^2 + \varphi\right)\right]}{\sqrt{\lambda_1 \lambda_2 \lambda_3}} \cdot \Phi_0\left(\frac{x}{\lambda_1}, \frac{y}{\lambda_2}, \frac{z}{\lambda_3}\right). \quad (3.25)$$

This scaling ansatz, holds as long as $V(\mathbf{r}, t)$ can be approximated by a quadratic potential around the COM, and where Φ_0 is the wavefunction at time $t = 0$ that satisfies Eq. 3.21 if the initial state was a stationary state in a trap. The λ_j are the scaling factors for each axis, $\alpha_j = \partial k_j / \partial r_j$ is the spatial derivative of the wavenumber which we call ‘‘momentum chirp’’, and φ is the global phase. The scaling factors, momentum chirp, and global phase are time dependent and are given in [45].

Visibility, coherence length and momentum coherence width

If Φ_0 is a Gaussian, or approximated by a Gaussian, the visibility is given by (Eq. 36 of [45])

$$V = \exp\left[-\frac{1}{2}\left(\sigma_z^2 \Delta \tilde{p}^2 / \hbar^2 + \Delta \tilde{z}^2 / 4\sigma_z^2\right)\right], \quad (3.26)$$

where σ_z is the initial wavepacket width before propagation and (Eq. 32 of [45])

$$\Delta \tilde{z} = \Delta z / \lambda_z, \quad \Delta \tilde{p} = \lambda_z \Delta p - m \dot{\lambda}_z \Delta z. \quad (3.27)$$

For the transverse scaling factor λ_z we have the form $\lambda_z(t) = \sqrt{1 + \omega_z^2 t^2}$, so $\dot{\lambda}_z = \omega_z^2 t / \lambda_z$. We also use $\hbar / 2m\omega_z = \ell_z^2$, where ℓ_z is the harmonic oscillator length along z , namely the width of a non-interacting atom in the ground state in the trap. We then obtain

$$V = \exp\left[-\frac{1}{2}\left(\frac{\sigma_z^2(1 + \omega_z^2 t^2)}{\hbar^2} \Delta p^2 + \frac{1 + \omega_z^2 t^2}{1 + \omega_z^2 t^2} \frac{(\sigma_z / \ell_z)^4 \Delta z^2}{4\sigma_z^2} - \frac{\sigma_z^2 \omega_z t}{\ell_z^2} \frac{\Delta z \Delta p}{\hbar}\right)\right]. \quad (3.28)$$

This equation describes the visibility of the SGI, given the final momentum and spatial splitting, initial parameters of the trap, and TOF. To better relate Eq. 3.28 to the experiment and render it more intuitive, we define the coherence length l_c as the spatial splitting at which $V = 1/e$ (for purely spatial splitting, i.e., $\Delta p = 0$), and the momentum coherence width l_p as the momentum splitting at which the visibility drops to $1/e$ (for purely momentum splitting, i.e., $\Delta z = 0$). Thus Eq. 3.28 can be written as

$$V = \exp\left[-\frac{\Delta p^2}{l_p(t)^2} - \frac{\Delta z^2}{l_c(t)^2} + \beta(t) \frac{\Delta z \Delta p}{\hbar}\right], \quad (3.29)$$

where

$$l_c = 2\sqrt{2}\sigma_z \sqrt{\frac{1 + \omega_z^2 t^2}{1 + \omega_z^2 t^2 (\sigma_z / \ell_z)^4}}, \quad (3.30)$$

$$l_p = \frac{\sqrt{2}\hbar}{\sigma_z \sqrt{1 + \omega_z^2 t^2}}, \quad (3.31)$$

and

$$\beta(t) = \frac{\sigma_z^2}{\ell_z^2} \omega_z t. \quad (3.32)$$

For $\Delta p = 0$, Eq. 3.29 gives

$$V(\Delta z)|_{\Delta p=0} = \exp \left[-\frac{\Delta z^2}{l_c(t)^2} \right] \quad (3.33)$$

and for $\Delta z = 0$ we obtain

$$V(\Delta p)|_{\Delta z=0} = \exp \left[-\frac{\Delta p^2}{l_p(t)^2} \right], \quad (3.34)$$

which are consistent with our definitions of the coherence length and momentum coherence width. These definitions enable experimental determinations of the coherence length and the momentum coherence width. A measurement of visibility as a function of spatial splitting, $V(\Delta z)$, should fit a Gaussian function $V(\Delta z) = V_0 \exp \left[-\frac{\Delta z^2}{l_c(t)^2} \right]$ and yield a value for the coherence length l_c . Similarly, a measurement of visibility as a function of momentum splitting gives a value for the momentum coherence width l_p . While measuring the coherence length, it is important to make sure that the momentum splitting Δp is minimal ($\Delta p \ll l_p$) so that the visibility drop is due to spatial splitting only; this can be ensured by optimizing the gradient pulses. Correspondingly, measuring the momentum coherence width requires ensuring that Δz is minimal by performing a very short sequence in which the spatial separation is negligible ($\Delta z \ll l_c$).

Chapter 4

Implementation of the full-loop Stern-Gerlach Interferometer

4.1 Experimental sequence

As described in the previous chapter, the Humpty-Dumpty effect (Eq. 3.29) requires that the eventual experimental imprecision in closing the loop (in position and momentum), should be smaller than the coherence length and the wavepacket width in momentum. Otherwise, the value of the overlap integral is small and the coherence, as observed through the interference visibility, will be small as well. This is a formidable task, and in the following I detail how it was achieved.

The experimental sequence is described in Fig. 4.1. The sequence consists of on-resonance RF pulses that manipulate the internal state of the atoms, and magnetic gradients that manipulate the momentum of these states. We start with a BEC, falling freely along the z -axis, in the $|2\rangle \equiv |F = 2, m_F = 2\rangle$ state, apply a $\pi/2$ RF pulse to create an equal superposition $\frac{1}{\sqrt{2}}(|1\rangle + |2\rangle)$, where $|1\rangle \equiv |F = 2, m_F = 1\rangle$. We then apply four magnetic gradients to split and recombine the wavepackets, with the two central pulses designed to stop and precisely reverse the wavepackets' momenta. The last pulse is intended to create overlap between the two wavepackets in both momentum and position.

Specifically, the first gradient (duration T_1) splits the wavepackets into two momentum states and determines the maximum momentum splitting Δp_{\max} . The delay time T_{d1} allows the wavepackets to separate spatially and determines the maximum spatial separation Δz_{\max} . After this delay time, a second gradient pulse (T_2) reverses the force applied to the wavepackets, thereby stopping their relative velocity. These first two gradient pulses complete the first half of the interferometer ($0 < t < T$). The second half of the interferometer ($T < t < 2T$) acts to recombine the wavepackets both in position and momentum. The third gradient pulse (T_3) follows immediately after the second pulse and reverses the momentum, the delay time T_{d2} closes the spatial separation, and the fourth pulse (T_4) closes the momentum separation, finally achieving a full-loop SGI with these four gradient pulses.

The four gradient pulses are generated by brief currents in the atom chip wires (the atom chip is described in Sec. 1.5). To get optimal recombination, it is necessary to adjust at least one gradient pulse (usually T_4 , or $T_2 + T_3$) and one delay time (T_{d2}). The optimization process is demonstrated in Fig. 4.2. Such an optimization is required since gravity, and mainly the magnetic force, increase the distance between the atom and the current-carrying wire as time evolves, and hence the magnetic gradients change even if exactly the same current is applied.

The measurement at the end of a sequence consists of a $\pi/2$ pulse, which projects the spin state onto the \hat{z} -axis of the Bloch sphere (which is defined by the strong homogeneous bias field along the y -axis in real space), after which a long gradient pulse separates the two states spatially and

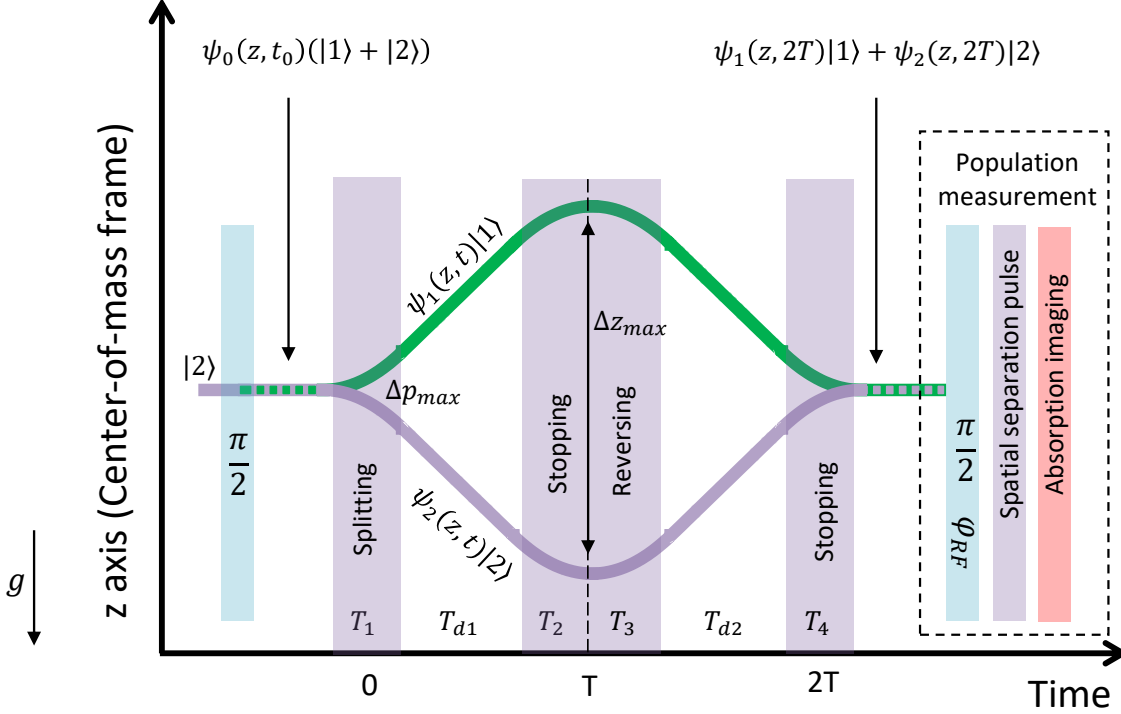


Figure 4.1: Experimental sequence of the longitudinal full-loop SGI (z position vs. time). The figure is plotted in the center-of-mass frame. The interferometer operates for a duration $2T$, and consists of four magnetic gradient pulses (purple columns) labeled by their respective durations T_1 - T_4 , with variable delay times T_{d1} and T_{d2} between them (there is no delay between T_2 and T_3). The states $|2\rangle \equiv |F=2, m_F=2\rangle$ and $|1\rangle \equiv |1, 1\rangle$ are defined along the Bloch sphere \tilde{z} -axis, while in real space the quantization axis is defined by the strong homogeneous bias field along the y -axis; the magnetic gradients and the interferometer axis are along the z -axis (direction of gravity). The simplest way to think about this interferometer is as a Ramsey sequence, with magnetic splitting in the middle. A more complex way to think about the interferometer, is that the experiment starts with an equal spin superposition in the \tilde{z} direction (on the Bloch sphere), namely, in the \tilde{x} direction (again on the Bloch sphere), and the final measurement is again of the spin in the \tilde{x} direction. The latter measurement (dotted rectangle) is performed by mapping the spins from \tilde{x} to \tilde{z} with a $\pi/2$ rotation (second blue columns) and applying a magnetic gradient pulse to separate the populations before taking an image (red column). The signal, measured at $t > 2T$, shows oscillations in the spin population. The first half of the interferometer ($0 < t < T$) determines the maximal splitting in position and momentum (Δz_{max} , Δp_{max}), while the second half ($T < t < 2T$) acts to recombine the wavepackets so that the final splitting in position and momentum [$\Delta z(2T)$, $\Delta p(2T)$] is minimal. This configuration requires high precision in order to maintain coherence; in contrast to the half-loop sequence realized previously, the full-loop SGI uses active recombination of the wavepackets.

an absorption image is taken. This procedure allows us to measure the relative population in each state (see Sec. 1.4 and Sec. 2.2.4). We can then determine the total phase difference $\Delta\Phi$ between the separated arms of the interferometer using Eq. 3.5.

To increase the coherence time and phase stability, we usually employ additional π pulses similar to the spin-echo method [47], see Fig. 4.3. The additional π pulses cancel effects of inhomogeneity in the magnetic bias field, and thus increase the visibility. The additional π pulses also eliminate phase fluctuations arising from detuning of the RF pulses, thus significantly increasing the shot-to-shot phase stability of the interferometer (see Sec. 2.2.3 and Appendix A for a detailed discussion).

It is also helpful to characterize the interferometer by applying the measurement part-way into the sequence. For example, measuring after the second pulse gives us information on the state of

the interferometer at the time of maximum spatial splitting Δz_{\max} , and measuring after the first pulse gives us information on the state of the interferometer at the time of maximum momentum splitting Δp_{\max} .

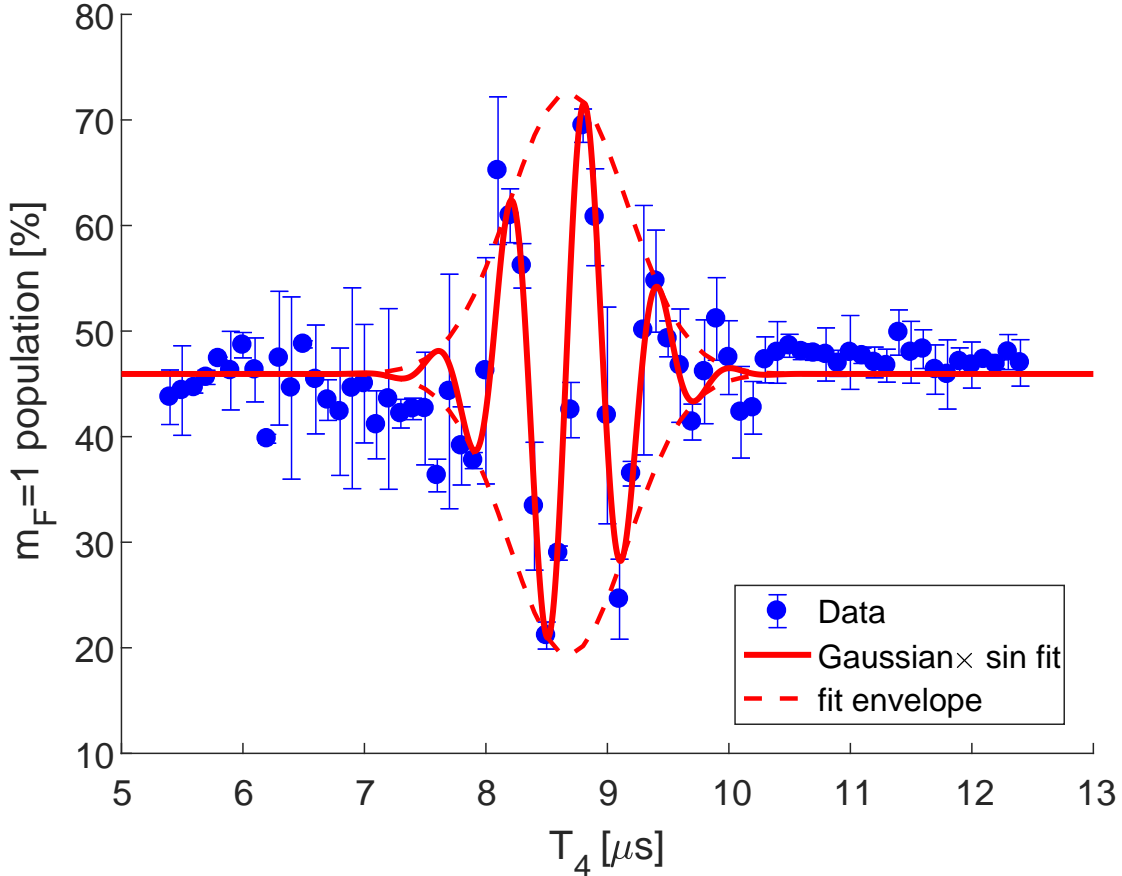


Figure 4.2: SGI optimization procedure. The population output is measured as a function of the pulse duration T_4 while other durations are fixed at $T_1 = 5.4 \mu\text{s}$, $T_2 = T_3 = 6.9 \mu\text{s}$, $T_{d1} = T_{d2} = 400 \mu\text{s}$. The population oscillates around the optimal point as expected by a model of a Gaussian times a sine function. The peak of the Gaussian envelope corresponds to the pulse duration of $T_4 = 8.7 \mu\text{s}$ for which the wavepacket overlap integral (Eq. 3.6) is maximized. The sine function corresponds to the added phase between the two interferometer arms as a function of gradient pulse duration T_4 .

4.2 Results

4.2.1 Coherence and splitting

As described in Sec. 3.4.3 and Eq. 3.29, the visibility of the spin population fringes should decrease as the final spatial separation increases or as the final momentum splitting increases, as this means that the overlap is reduced. In next sections we measure the visibility as a function of the final spatial separation, in order to confirm this relation and to measure the coherence length of the wavepacket. We accomplish this by applying only two gradient pulses T_1, T_2 with a delay time T_{d1} between them. In addition, we perform a separate series of measurements to confirm the successful recombination by observing the regained visibility (revival) as we add the recombining pulses T_3, T_4 with delay time T_{d2} .

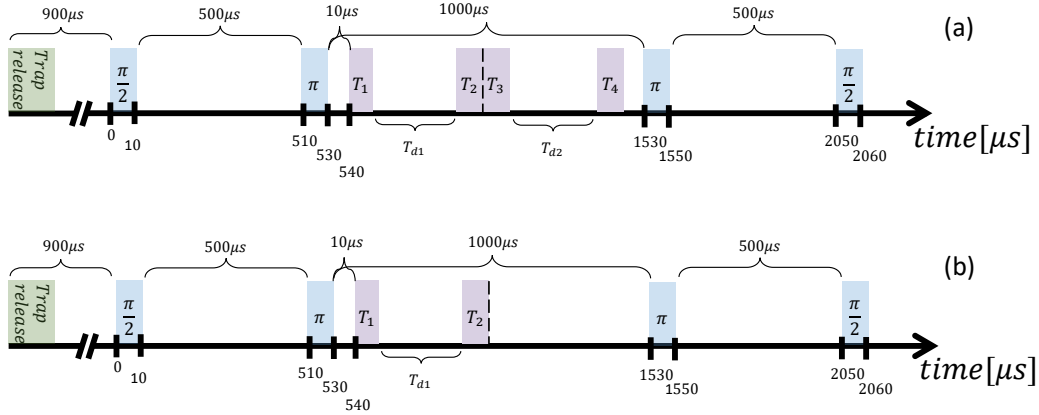


Figure 4.3: Experimental sequence and timing, full-loop and double kick. (a) Full loop with dynamical decoupling RF sequence, the two π pulses increase the coherence and stability of the spin signal. (b) Double kick with dynamical decoupling RF sequence, this sequence measures the state of the SGI with maximal spatial splitting. The duration T_2 is optimized for maximal visibility.

4.2.2 Demonstrating active recombination

To successfully achieve spin population fringes in the full-loop SGI, one has to effectively split and recombine the wavepackets. Here we demonstrate the effect of the splitting and recombination in the SGI. The splitting is demonstrated by applying two gradient pulses of duration T_1, T_2 with a delay time T_{d1} between them (Fig. 4.4 blue data). As we extend the delay time T_{d1} the wavepackets start to split in space and we observe a decay in visibility which cannot be restored using T_2 alone, as the distance between the wavepackets becomes larger than their coherence length l_c . We validate that this loss of visibility is mainly due to spatial splitting (and not momentum splitting), by optimizing T_2 for each value of T_{d1} , whereby T_2 is responsible for zeroing the relative momentum. This is explained further in the following subsection.

Separately, we measure the signal at $t = 2T$, after employing the two recombination pulses T_3, T_4 , while observing the visibility after recombination (Fig. 4.4 red data). The value of T_4 is optimized for each value of T_{d1} and T_{d2} (which are equal to each other), such that maximal visibility is achieved. One can clearly see the Gaussian decay of the visibility due to spatial splitting in the first (blue) data, and the revival of the visibility due to the successful recombination of the spatially-split wavepackets (red data). The improved visibility after adding the recombination pulses verifies their effectiveness.

In summary, we have clearly shown the successful recombination in momentum and position, thus realizing a complete SGI.

4.2.3 Coherence length

Fig. 4.4 shows a measurement of the state of the SGI half way through the sequence at $t = T$ when the spatial splitting is maximal. We get an experimental measurement of the coherence length of the cloud by fitting the envelope of the oscillations in Fig. 4.4 and extracting the value at which the visibility decays to $1/e$ of its initial value. This procedure gives a coherence length of $l_c = 0.7 \pm 0.1 \mu\text{m}$. This stands in some contrast with the theoretical prediction of Eq. 3.30, which yields $l_c \approx 1.2 \mu\text{m}$ for our experimental parameters ($\sigma_z = 1.2 \mu\text{m}$, $\omega_z = 2\pi \times 120 \text{ Hz}$, $t = 3.5 \text{ ms}$, and $\ell_z = 0.7 \mu\text{m}$), and may result from a thermal component in the BEC. We verify that the loss of visibility in this measurement is due to spatial splitting by minimizing the visibility loss due to momentum splitting for each value of T_{d1} , using the following optimization procedure. We scan for

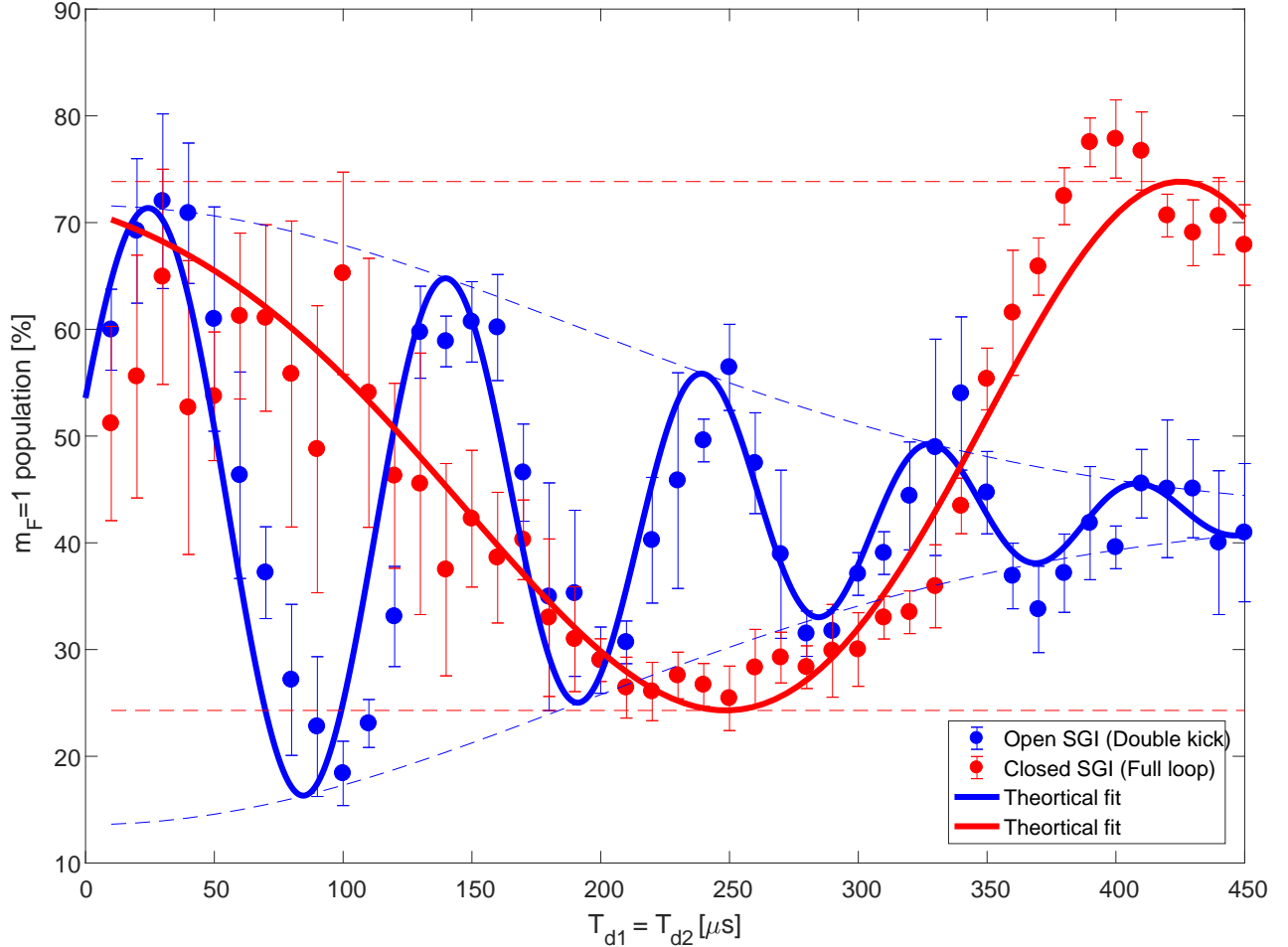


Figure 4.4: Effective recombination in the SGI and phase of the SGI. In blue, measuring the state of the SGI half way through the sequence at $t = T$ when the spatial splitting is maximal. In red, measuring the full-loop, after recombination of the wavepackets. The data show the drop in visibility due to spatial splitting, and revival of visibility due to effective recombination. For the blue data, we make sure that the visibility drop due to momentum difference is minimal by optimizing the stopping pulse T_2 , and in the full-loop optimizing T_4 as well (see Fig. 4.2 as an example for optimization). The specific sequence is presented in Fig. 4.3. The blue data set is fitted to a decaying oscillation of the form $V_0 e^{(-T_{d1}^2/\tau^2)} \sin(\Delta\phi_{\text{open}} + \varphi_0) + d$, from which we get a decay time of $\tau = 270 \pm 30 \mu\text{s}$, which gives the coherence length $l_c = \Delta a T_1 \tau = 0.7 \pm 0.1 \mu\text{m}$ where $\Delta a = 460 \pm 10 m/s^2$ is the differential acceleration of the wavepackets during T_1 . The red data is fitted to an oscillation of the form $V_0 \sin(\Delta\phi_{\text{closed}} + \varphi_0) + d$. The phase $\Delta\phi_{\text{open}}$ is given by Eq. 3.19, and $\Delta\phi_{\text{closed}}$ by Eq. 3.15 [43].

the optimal value of T_2 , i.e., the value which produces the maximal visibility for each delay time ($T_{d1} = 100, 200, 300, 400 \mu\text{s}$), in a manner similar to what is shown in Fig. 4.2. We then determine the optimal T_2 for any given value of T_{d1} by using a polynomial interpolation. The blue data in Fig. 4.3 is taken by using the optimal values of T_2 as a function of T_{d1} . This ensures that the visibility loss due to momentum splitting is minimized for every value of T_{d1} , meaning that the visibility loss is mostly due to spatial splitting.

4.2.4 Momentum coherence width

Here we measure the effect of momentum splitting on the visibility of the full-loop SGI. Figure 4.5 presents such a measurement, showing the loss of coherence due to the first magnetic pulse alone (i.e., by setting $T_2, T_3, T_4 = 0$), giving rise to orthogonality in momentum. For this purpose, we expose the atoms prepared in the state $|+\tilde{x}\rangle = \frac{1}{\sqrt{2}}(|1\rangle + |2\rangle)$, to a single magnetic gradient kick, and we measure the spin population in the \tilde{x} direction (same measurement as in Fig. 4.1) before the two wavepackets have time to spatially separate. Any loss of coherence thus originates from orthogonality in momentum. The wavepackets become orthogonal in momentum at $l_p/m = 0.11 \pm 0.02$ mm/s relative velocity, where m is the atomic mass, and l_p is the measured momentum coherence width defined in Eq. 3.34. We note that, to the best of our knowledge, this is the first direct measurement of the momentum coherence width of a BEC, where advantage was taken of the fact that we are not limited to the quantized momentum kick of a single photon, as in interferometers based on light.

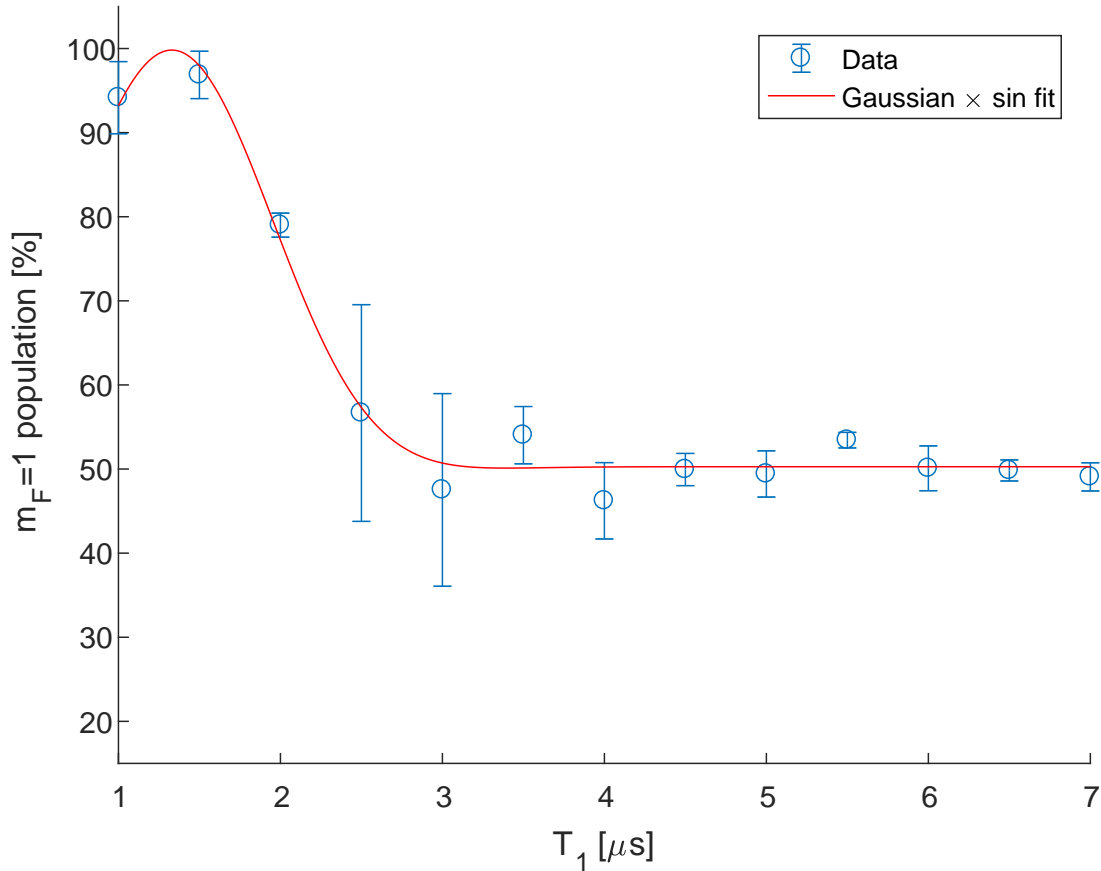


Figure 4.5: Single kick effect on the visibility: population as a function of the duration of a single first gradient pulse T_1 (where we set $T_2, T_3, T_4 = 0$). As T_1 is increased, the population decays to 50% - corresponding to zero visibility. In this measurement we take care that the spatial separation is as small as possible ($\Delta z \leq 70$ nm) such that the decay due to spatial splitting is negligible (less than 1%). The velocity difference is calculated according to $\Delta v = aT_1$, where $a = 130$ m/s² is the applied relative acceleration. The data is fitted to a Gaussian times a sine function, and the fit returns a decay time $\tau = 0.86$ μs , which corresponds to a momentum coherence width of $l_p/m = 0.11 \pm 0.02$ mm/s, where m is the atomic mass. As in Fig. 4.2, the Gaussian describes the decreasing overlap and the sine describes the evolving relative phase due to the magnetic potential induced by the gradient pulse.

4.2.5 Momentum coherence width and temperature

Finally, we show preliminary work on measuring the dependence of the momentum coherence width on the atom number, temperature of the cloud, and its size. It is not intended to be a quantitative description but rather a demonstration that there is a dependence that can be observed experimentally. Changing the value of the last RF ramp in the evaporation cooling process affects the atom number, temperature of the cloud, and its size. Specifically, lowering the last RF ramp value lowers all three (see Fig. 4.6).

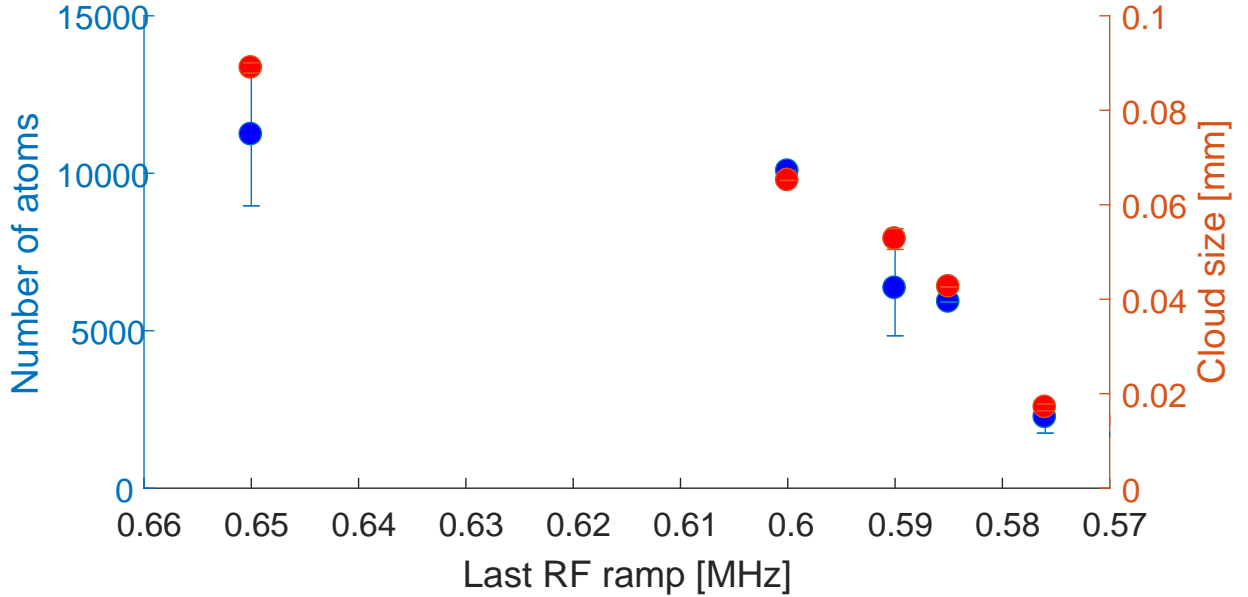


Figure 4.6: Number of atoms and cloud size (z -axis) vs. last RF ramp. The cloud size is measured at 16 ms TOF after the trap release.

As the last RF ramp approaches the trap bottom, fewer atoms are left in the trap, the cloud’s temperature decreases, and it gets smaller. The visibility depends on l_c , l_p and β , (see Eq. 3.29), which all depend on the cloud size σ_z . So for a given momentum splitting, the visibility is predicted to be higher for a smaller cloud. The results of this measurement are presented in Fig. 4.7, measuring the loss of coherence due to momentum splitting for different values of the last RF ramp. The results show a clear trend, in which the lowest RF ramp shows the lowest loss of coherence for a given momentum splitting, implying that lowering the last RF ramp indeed increases l_p . For a quantitative discussion of these relations, more data and analysis are required, which is beyond the scope of this work. This effect can be exploited in the future to improve the coherence of the full-loop SGI and reduce its sensitivity to inaccuracies in the recombination.

4.3 Phase noise

As detailed in the above chapter, the main challenge addressed by my M.Sc. work is the HD effect, namely, achieving the necessary accuracy to maintain coherence. However, other, more “mundane” issues also have to be addressed in order to observe a good signal. Specifically, one also needs to address the issue of stability, whereby temporal fluctuations may give rise to dephasing and drifts. Even in the absence of environmentally induced decoherence, noise may cause the interference phase to jitter from one experimental shot to the next (e.g., due to a fluctuating bias field), thus dephasing the averaged phase. This shot-to-shot phase noise gives rise to population noise, where spin population is our main observable. In the lab, we made a significant effort to detect and

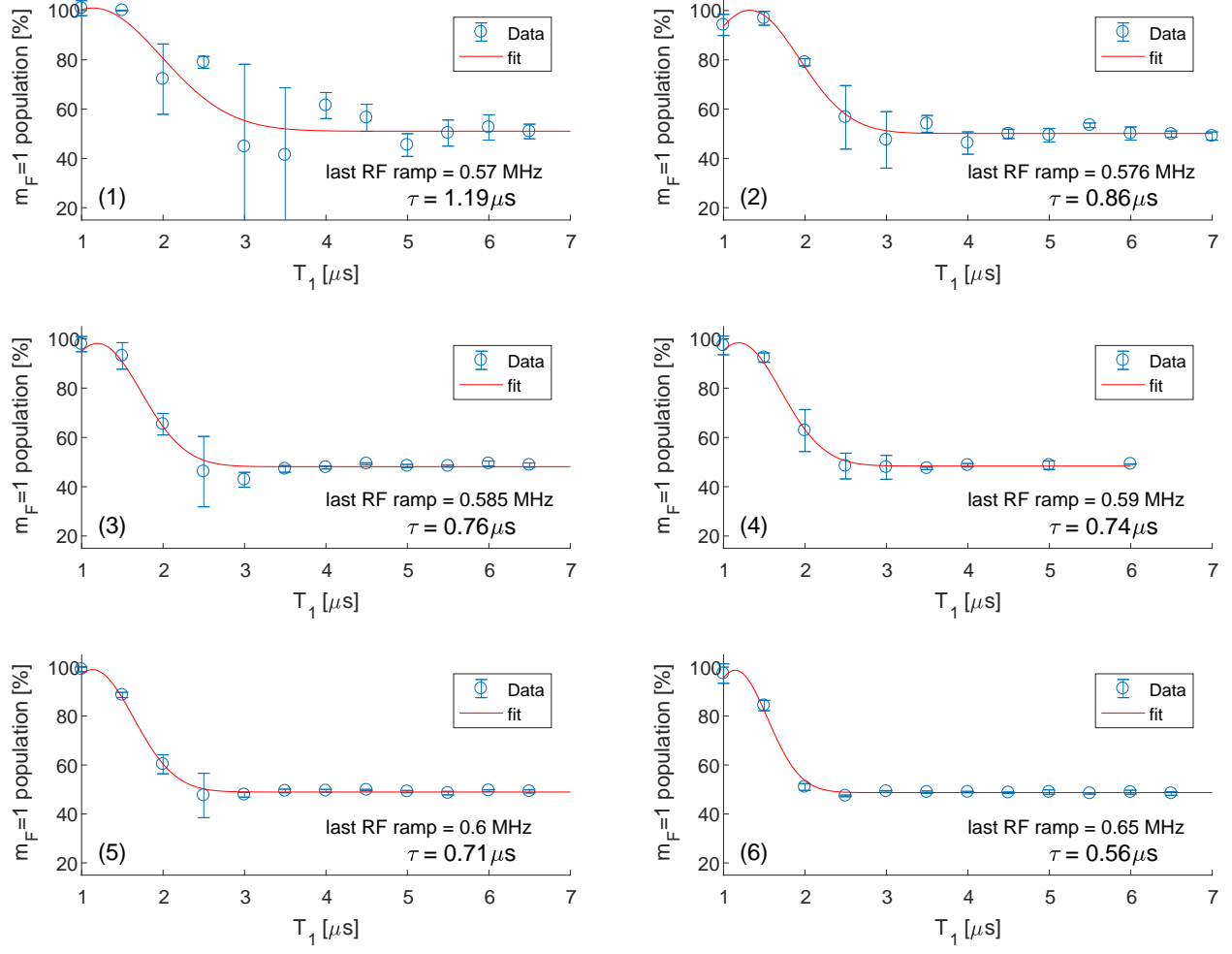


Figure 4.7: Momentum coherence width and temperature. Measuring the visibility decay as a function of the momentum splitting for 6 different evaporative cooling ramps. (1) The last RF ramp is set to 0.57 MHz, and the decay constant is $\tau = 1.19 \mu\text{s}$. (2-6) Increasing the last RF ramp value (0.576, 0.585, 0.59, 0.60, 0.65) MHz, i.e., increasing the cloud temperature, size, and number of atoms, shortens the decay time ($\tau = 0.86, 0.76, 0.74, 0.71, 0.56 \mu\text{s}$). The six decay times correspond to momentum coherence widths of $l_p/m = 0.16, 0.11, 0.10, 0.10, 0.09, 0.07 \text{ mm/s}$ respectively.

suppress the different sources of noise. In Appendix A we detail our simulations and estimations of our main noise sources.

Chapter 5

Summary and Outlook

To conclude, we have demonstrated for the first time a full-loop SGI, consisting of freely propagating atoms exposed to magnetic gradients, as originally envisioned decades ago. We have unambiguously shown recombination in both momentum and position. We have shown that SG splitting may be realized in a highly coherent manner with macroscopic magnets without requiring cryogenic temperatures or magnetic shielding.

We measured the coherence length of the wavepacktes in the SGI and presented a measurement of the momentum coherence width which is, to the best of our knowledge, the first time it has been measured directly.

We measured the phase accumulation of an open SGI configuration and verified the theoretical prediction for this phase including the prediction for the separation phase. We suggested a method for isolating the separation phase contribution from other parts of the phase by subtracting the phase of two interferometric schemes.

The measurements of the coherence length and momentum coherence width may allow us to accurately predict the visibility of the full-loop in different interferometric schemes and configurations, a challenge we have yet to overcome [6], and may help to further improve our control and accuracy in the recombination.

The methods we introduced allow for many variations and novel interferometric schemes, such as the T^3 SGI interferometer realized in [43] by setting the delay time between the gradient pulses to zero, and a T^n interferometer which is feasible by controlling the temporal shape of the gradient pulses.

Furthermore, as the SGI does not require light, it can be operated close to surfaces, and consequently can be applied for probing surface physics, such as interferometric measurements of Johnson noise and the Casimir-Polder force near the atom chip, or even searches for the hypothesized fifth force. It could also be used for ultra-sensitive probing of electron transport down to shot-noise and squeezed currents [48].

Another benefit of the SGI in comparison to light-based atom interferometers is the ability to manipulate the internal degrees of freedom (Zeeman sub-levels) without affecting the external degrees of freedom (momentum and position). Variations on the number of RF pulses and their timings, and similar variations on the gradient pulses, will allow for more interferometric configurations; for example, a butterfly configuration whose phase is not sensitive to gravity [44] is attainable by simply adding two more gradient pulses with the appropriate timing. An interferometer with multiple trajectories may be possible by using the 5 Zeeman substates of the $F = 2$ ground state. It is also possible to have two simultaneous interferometers in one experimental cycle by establishing and manipulating two independent two-level systems, each with its own resonance frequency, thus allowing for differential measurements.

The full-loop SGI has been suggested as an experimental test for Einstein's equivalence principle when extended to the quantum domain [49]. SG interferometry with mesoscopic objects has been

suggested as a compact detector for the space-time metric and curvature [50], possibly enabling detection of gravitational waves. It has also been suggested as a probe for the quantum nature of gravity [51].

It seems we have just started to explore the possibilities embedded in the Stern-Gerlach interferometer. I am hopeful that my work will help open the door for a wide variety of future experiments.

Bibliography

- [1] A. D. Cronin, J. Schmiedmayer, and D. E. Pritchard, “[Optics and interferometry with atoms and molecules,](#)” *Rev. Mod. Phys.* **81**, 1051–1129 (2009).
- [2] M. J. Snadden, J. M. McGuirk, P. Bouyer, K. G. Haritos, and M. A. Kasevich, “[Measurement of the Earth’s Gravity Gradient with an Atom Interferometer-Based Gravity Gradiometer,](#)” *Phys. Rev. Lett.* **81**, 971–974 (1998).
- [3] R. H. Parker, C. Yu, W. Zhong, B. Estey, and H. Müller, “[Measurement of the fine-structure constant as a test of the Standard Model,](#)” *Science* **360**, 191–195 (2018).
- [4] J. Baudon, R. Mathevet, and J. Robert, “[Atomic interferometry,](#)” *J. Phys. B* **32**, R173–R195 (1999).
- [5] S. Machluf, Y. Japha, and R. Folman, “[Coherent Stern–Gerlach momentum splitting on an atom chip,](#)” *Nature Commun.* **4**, 2424 (2013).
- [6] Y. Margalit, Z. Zhou, O. Dobkowski, Y. Japha, D. Rohrlich, S. Moukouri, and R. Folman, “[Realization of a complete Stern-Gerlach interferometer,](#)” arXiv:1801.02708 (2018).
- [7] Y. Margalit, Z. Zhou, S. Machluf, Y. Japha, S. Moukouri, and R. Folman, “[Analysis of a high-stability Stern-Gerlach spatial fringe interferometer,](#)” *New J. Phys.* **21**, 073040 (2019).
- [8] B. G. Englert, J. Schwinger, and M. O. Scully, “[Is spin coherence like Humpty-Dumpty? I. Simplified treatment,](#)” *Found. Phys.* **18**, 1045–1056 (1988).
- [9] J. Schwinger, M. O. Scully, and B. G. Englert, “[Is spin coherence like Humpty-Dumpty? - II. General theory,](#)” *Z. Phys. D* **10**, 135–144 (1988).
- [10] M. O. Scully, B. G. Englert, and J. Schwinger, “[Spin coherence and Humpty-Dumpty. III. the effects of observation,](#)” *Phys. Rev. A* **40**, 1775–1784 (1989).
- [11] S. Machluf, “[Coherent Splitting of Matter-Waves on an Atom Chip Using a State-Dependent Magnetic Potential,](#)” Ph.D. thesis (2013).
- [12] S. Machluf, “[Building a BEC on an atom chip apparatus,](#)” Master’s thesis (2009).
- [13] Y. Margalit, “[Stern-Gerlach Interferometry with Ultracold Atoms,](#)” Ph.D. thesis (2018).
- [14] D. A. Steck, “[Rubidium 87 D Line Data,](#)” (2010).
- [15] M. Keil, O. Amit, S. Zhou, D. Groswasser, Y. Japha, and R. Folman, “[Fifteen years of cold matter on the atom chip: promise, realizations, and prospects,](#)” *J. Mod. Opt.* **63**, 1840–1885 (2016).

- [16] P. B. Wigley, P. J. Everitt, A. van den Hengel, J. W. Bastian, M. A. Sooriyabandara, G. D. McDonald, K. S. Hardman, C. D. Quinlivan, P. Manju, C. C. N. Kuhn, I. R. Petersen, A. N. Luiten, J. J. Hope, N. P. Robins, and M. R. Hush, “Fast machine-learning online optimization of ultra-cold-atom experiments,” *Scientific Reports* **6**, 25890 (2016).
- [17] T. David, “Magnetic interactions of ultra-cold atoms near surfaces,” Ph.D. thesis (2009).
- [18] R. Salem, “Bose-Einstein Condensate on the Atom Chip,” Ph.D. thesis (2010).
- [19] S. Wildermuth, P. Krüger, C. Becker, M. Brajdic, S. Haupt, A. Kasper, R. Folman, and J. Schmiedmayer, “Optimized magneto-optical trap for experiments with ultracold atoms near surfaces,” *Phys. Rev. A* **69**, 030901 (2004).
- [20] H. J. Metcalf, “Laser cooling and trapping of atoms,” *J. Opt. Soc. Am. B* **20** (2003).
- [21] A. L. Migdall, J. V. Prodan, W. D. Phillips, T. H. Bergeman, and H. J. Metcalf, “First Observation of Magnetically Trapped Neutral Atoms,” *Phys. Rev. Lett.* **54**, 2596–2599 (1985).
- [22] R. Folman, P. Krger, J. Schmiedmayer, J. Denschlag, and C. Henkel, “Microscopic atom optics: from wires to an atom chip,” *Adv. At. Mol. Opt. Phys.* **48**, 263 – 356 (2002).
- [23] W. Ketterle and N. V. Druten, “Evaporative Cooling of Trapped Atoms,” (Academic Press, 1996), pp. 181 – 236.
- [24] F. Dalfovo, S. Giorgini, L. P. Pitaevskii, and S. Stringari, “Theory of Bose-Einstein condensation in trapped gases,” *Rev. Mod. Phys.* **71**, 463–512 (1999).
- [25] E. L. Hahn, “Spin Echoes,” *Phys. Rev.* **80**, 580–594 (1950).
- [26] W. Gerlach and O. Stern, “The experimental proof of directional quantization in the magnetic field,” *Z. Physik* **9**, 349–352 (1922).
- [27] J. Robert, C. H. Miniatura, S. L. Boiteux, J. Reinhardt, V. Bocvarski, and J. Baudon, “Atomic interferometry with metastable hydrogen atoms.” *EPL* **16**, 29–34 (1991).
- [28] C. Miniatura, F. Perales, G. Vassilev, J. Reinhardt, J. Robert, and J. Baudon, “A longitudinal stern-gerlach interferometer : the beaded atom,” *Journal de Physique II* **1**, 425–436 (1991).
- [29] C. Miniatura, J. Robert, S. L. Boiteux, J. Reinhardt, and J. Baudon, “A longitudinal stern-gerlach atomic interferometer,” *Applied Physics B* **54**, 347–350 (1992).
- [30] J. Robert, C. Miniatura, O. Gorceix, S. L. Boiteux, V. Lorent, J. Reinhardt, and J. Baudon, “Atomic quantum phase studies with a longitudinal stern-gerlach interferometer,” *Journal de Physique II* **2**, 601–614 (1992).
- [31] C. Miniatura, J. Robert, O. Gorceix, V. Lorent, S. L. Boiteux, J. Reinhardt, and J. Baudon, “Atomic interferences and the topological phase,” *Physical Review Letters* **69**, 261–264 (1992).
- [32] S. N. Chormaiet, V. Wiedemann, C. Miniatura, J. Robert, S. L. Boiteux, V. Lorent, O. Gorceix, S. Feron, J. Reinhardt, and J. Baudon, “Longitudinal stern-gerlach atomic interferometry using velocity selected atomic beams,” *J. Phys. B* **26**, 1271–1279 (1993).
- [33] J. Baudon, R. Mathevet, and J. Robert, “Atomic interferometry,” *J. Phys. B* **32**, R173 (1999).
- [34] M. Boustimi, V. Bocvarski, B. V. de Lesegno, K. Brodsky, F. Perales, J. Baudon, and J. Robert, “Atomic interference patterns in the transverse plane,” *Phys. Rev. A* **61**, 6 (2000).

- [35] E. Marchal, R. Long, T. Miossec, J. L. Bossennec, R. Barb, J. C. Keller, and O. Gorceix, “[Atomic spatial coherence monitoring and engineering with magnetic fields,](#)” *Phys. Rev. A* **62**, 053603–053601 (2000).
- [36] B. V. de Leseqno, J. C. Karam, M. Boustimi, F. Perales, C. Mainos, J. Reinhardt, J. Baudon, V. Bocvarski, D. Grancharova, F. P. D. Santos, T. Durt, H. Haberland, and J. Robert, “[Stern gerlach interferometry with metastable argon atoms: An immaterial mask modulating the profile of a supersonic beam,](#)” *Eur. Phys. J. D* **23**, 25–34 (2003).
- [37] M. Chen, K. A. Rubin, and R. W. Barton, “[Compound materials for reversible, phase-change optical data storage,](#)” *Appl. Phys. Lett.* **49**, 502–504 (1986).
- [38] Y. Margalit, Z. Zhou, S. Machluf, D. Rohrlich, Y. Japha, and R. Folman, “[A self-interfering clock as a “which path” witness,](#)” *Science* **349**, 1205–1208 (2015).
- [39] Z. Zhou, Y. Margalit, D. Rohrlich, Y. Japha, and R. Folman, “[Quantum complementarity of clocks in the context of general relativity,](#)” *Class. Quantum Grav.* **35**, 185003 (2018).
- [40] B.-G. Englert, “[Fringe visibility and which-way information: An inequality,](#)” *Phys. Rev. Lett.* **77**, 2154–2157 (1996).
- [41] Z. Zhou, Y. Margalit, S. Moukouri, Y. Meir, and R. Folman, “[An experimental test of the geodesic rule proposition for the noncyclic geometric phase,](#)” *Science Advances* **6** (2020).
- [42] D. Bohm, *Quantum theory* (Englewood Cliffs, N.J. : Prentice-Hall, 1951), pp. 604–605.
- [43] O. Amit, Y. Margalit, O. Dobkowski, Z. Zhou, Y. Japha, M. Zimmermann, M. A. Efremov, F. A. Narducci, E. M. Rasel, W. P. Schleich, and R. Folman, “ [\$T^3\$ stern-gerlach matter-wave interferometer,](#)” *Phys. Rev. Lett.* **123**, 083601 (2019).
- [44] G. D. McDonald and C. C. N. Kuhn, “[Space-Time Area in Atom Interferometry,](#)” arXiv:1312.2713 (2013).
- [45] Y. Japha, “[Generalized wave-packet model for studying coherence of matter-wave interferometers ,](#)” arXiv:1902.07759v2 (2020).
- [46] A. Roura, W. Zeller, and W. P. Schleich, “[Overcoming loss of contrast in atom interferometry due to gravity gradients,](#)” *New J. Phys.* **16**, 123012 (2014).
- [47] E. L. Hahn, “[Spin Echoes,](#)” *Phys. Rev.* **80**, 580–594 (1950).
- [48] N. Y. D. V. Strekalov and K. Mansour, “[Sub-Shot Noise Power Source for Microelectronics,](#)” NASA Tech Briefs (2011).
- [49] C. Marletto and V. Vedral, “[On the testability of the equivalence principle as a gauge principle detecting the gravitational \$t_3\$ phase,](#)” *Front. Phys.* **8**, 176 (2020).
- [50] R. J. Marshman, A. Mazumdar, G. W. Morley, P. F. Barker, S. Hoekstra, and S. Bose, “[Mesoscopic interference for metric and curvature & gravitational wave detection,](#)” *New J. Phys.* **22**, 083012 (2020).
- [51] S. Bose, A. Mazumdar, G. W. Morley, H. Ulbricht, M. Toroš, M. Paternostro, A. A. Geraci, P. F. Barker, M. S. Kim, and G. Milburn, “[Spin entanglement witness for quantum gravity,](#)” *Phys. Rev. Lett.* **119**, 240401 (2017).

Appendices

Appendix A

Phase noise analysis

In this appendix I present an analysis of the shot-to-shot phase noise in a Ramsey sequence, and its relation to the noise in the population output. The issue of instability, whereby temporal fluctuations may give rise to dephasing and drifts, and cause the interference phase to jitter from one experimental shot to the next (e.g., due to a fluctuating bias field) is addressed. This shot-to-shot phase noise gives rise to population noise. As an example for population noise we present in Fig. A.1 two population measurements with some phase noise.

As the observable of our measurement is population, one cannot get a direct measurement of the shot-to-shot phase noise. Due to the trigonometric relation of population to phase given in Eq. 3.5, the mathematics of translating the phase fluctuations into population fluctuations has some interesting and non-intuitive characters. In this appendix, we present numerical simulations that provide insight and suggest a way to quantitatively estimate the shot-to-shot phase stability of a system by measuring the population vs. Ramsey time, and fitting the data to a numerical simulation.

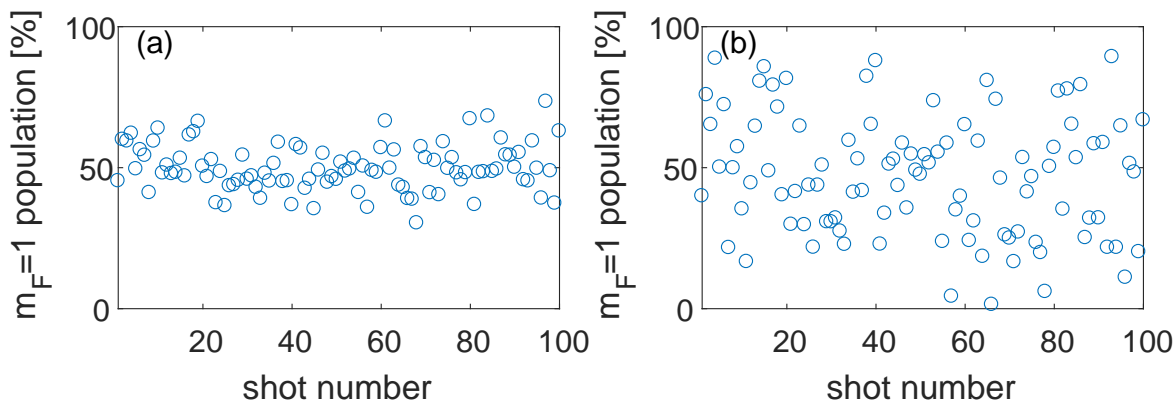


Figure A.1: A simulation of two noisy population measurements demonstrating shot-to-shot phase noise, with a mean population $P_{\text{mean}} = 0.5$. The phase distribution may take on different forms (see Fig. A.2).

A.1 Phase noise simulation

A.1.1 Model

The relation between the phase and population given by Eq. 3.5 is $P_1 = \frac{1}{2}[1 + V \cos(\phi)]$, where ϕ is the total phase and V is the visibility of the population oscillation which we set to $V = 1$ in this discussion. To simulate phase noise, we assume ϕ to be a random variable with a normal distribution,

with a mean phase ϕ_{mean} and standard deviation σ_ϕ , so that $\phi = \frac{1}{\sigma_\phi \sqrt{2\pi}} \exp\left[-\frac{1}{2} \left(\frac{\phi - \phi_{\text{mean}}}{\sigma_\phi}\right)^2\right]$. This is a reasonable assumption as many experimental noise sources can be well approximated by a normal distribution. For the numerical simulation we create a set of randomly distributed phases with mean and standard deviation $\phi_{\text{mean}}, \sigma_\phi$ (using Matlab's normal random number generator), and then calculate $P(m_F = 1)$ for each random phase. From this data set we calculate the mean population P_{mean} and standard deviation $\sigma_P = \sqrt{\frac{1}{n} \sum_{i=1}^n (P_i - P_{\text{mean}})^2}$. Since P does not have a normal distribution, σ_P is not the width of the distribution, but simply the standard deviation. Results from this simple simulation are presented in Fig. A.2, in the form of a scatter plot and histogram for different σ_ϕ .

Figure A.3 shows the relation of σ_P vs. σ_ϕ , for different ϕ_{mean} . The population spread σ_P starts with a linear relation to σ_ϕ and reaches an asymptote with a maximal value of $\sigma_P \approx 35\%$. Using this plot and the values of P_{mean} and σ_P one can extract the value of σ_ϕ . However, due to the asymptomatic relation for large phase noise, when $\sigma_\phi > 60^\circ$, the phase noise cannot be reliably estimated with such a method.

Figure A.4 demonstrates the effect of σ_ϕ on a phase scan by showing four phase scans with different phase noise. The phase noise lowers the visibility of the oscillation, and of course increases the error bars. Averaging a large number of shots (> 10) allows us to obtain a signal even with $\sigma_\phi = 60^\circ$ or more. The size of the error bars oscillates along the phase scan (for $\sigma_\phi < 60^\circ$), where the oscillation of the size of the error bars may be considered a footprint of phase noise. In principle it is possible to extract the phase noise from such a measurement by fitting the size of error bars to a model, but in practice this approach will be beneficial only for rather small phase noise, and will require a fine phase scan with a large number of iterations per point to get a valid estimation for significant phase noise. Next, we suggest and implement a more effective way of estimating the shot-to-shot phase stability of the experiment.

A.1.2 Measuring the shot-to-shot phase stability

Sources for phase fluctuations

The phase in a Ramsey scheme (Sec. 2.2.3) is given by $\phi = \int_0^{T_R} \delta\omega dt$ where $\delta\omega = 2\pi(f_{RF} - f_0)$ is the detuning of the RF pulses from the atomic resonance frequency, f_0 , where in our system, $f_0 = \Delta[-\boldsymbol{\mu} \cdot \mathbf{B}]/h = 24.6$ MHz. The Ramsey time T_R is the interval between the two RF pulses (typically in the range of 50–500 μs in our system). Shot-to-shot phase noise is due to low frequency noise, such that $f_{\text{noise}} \ll \frac{1}{T_R}$; for this condition $\delta\omega$ is constant during T_R and the integral becomes a simple multiplication

$$\phi = \delta\omega \times T_R. \quad (\text{A.1})$$

We can also electronically add a phase shift between the two $\pi/2$ RF pulses, φ_{RF} , and we obtain $\phi = \delta\omega \times T_R + \varphi_{\text{RF}}$. From this equation we can count the different sources for shot-to-shot phase noise: RF signal frequency fluctuations will affect $\delta\omega$, RF pulse timing jitter will affect T_R , RF signal phase fluctuations will affect φ_{RF} . These noise sources are assumed to be negligible as the RF signal generator contains an atomic clock, which stabilizes the RF frequency and phase, and is synchronized to the PXI that controls the duration of the pulses. Consequently, we can conclude that the multi-shot stability of the experiment depends on the frequency stability of the superposition itself which is linear with the magnitude of the magnetic bias field. The magnetic field fluctuations cannot be directly measured in a straightforward way. The magnetic field noise is mainly affected by current fluctuations in the power supply, whose usual stability is $10^{-5} < \frac{\delta I}{I} < 10^{-4}$. Directly measuring the stability of the power supply is at the limit of accuracy of the measuring device we use (LEM IT 100-S current sensor with $8.4 \cdot 10^{-5}$ sensitivity, connected to a Keithley 2000 multimeter). The only thing in the lab that is more accurate and sensitive to current and magnetic field are the

atoms themselves so in the following we use them to measure the stability of the field.

Quantitative estimation of the field stability

Observing the relation $\phi = \delta\omega \times T_R$, one can see that fluctuations of $\delta\omega$ are multiplied by the Ramsey time T_R , and consequently, the shot-to-shot phase fluctuations should be linear with T_R . Measuring these fluctuations as a function of the Ramsey time can give information on the stability of $\delta\omega$. If the main noise source is the magnetic field, the stability of this field can be measured with such a procedure (or the stability of detuning in a more general view). To conclude, increasing T_R will not only show the expected decaying population oscillation (decaying due to decoherence and inhomogeneity in the bias field during the Ramsey sequence¹), but should also show an increasing size of the error bars (σ_P). Using the relation between the error bars and the Ramsey time, we suggest a method for measuring the field stability by measuring the size of the error bars in a Ramsey scheme vs. the duration of the Ramsey time T_R . The model is as follows: the population of the $m_F = 1$ state in a Ramsey sequence is given by

$$P(m_F = 1) = 0.5 + 0.5 \exp\left(-\frac{t}{\tau_R}\right) \cos(\delta\omega \times T_R + \phi_0), \quad (\text{A.2})$$

where $\delta\omega$ is the detuning, τ_R is the coherence time of the Ramsey sequence (not to be confused with decay constant τ from Ch. 4), T_R is the time between the two RF pulses, and ϕ_0 is the initial phase. To simulate the shot-to-shot phase noise, we define $\delta\omega$ to be a random normal variable with a mean $\delta\omega_{\text{mean}} = 2\pi(f_{\text{RF}} - f_0)$ and standard deviation $\sigma_{\delta\omega}$. This model has 4 free parameters, $\tau_R, \phi_0, \delta\omega$, and $\sigma_{\delta\omega}$. While fitting the model with its 4 free parameters we estimate the goodness of the fit between the model and data by the value of $R^2 = 1 - \frac{SS_{\text{res}}}{SS_{\text{tot}}}$ where $SS_{\text{res}} = \sum_i (P_i - y_i)^2$ (sum of squares of the residuals, P_i are simulation results and y_i are the experimental data points) and $SS_{\text{tot}} = \sum_i (y_i - \bar{y})^2$ (total sum of squares). The 4 parameters are first set by hand to reach a reasonable fit, and then optimized so that R^2 is maximized using the M-loop optimization algorithm [16].

Results

The results are presented Fig. A.5 showing the experimental data (blue) and the numerical simulation of the model (red). The data shows a decaying population oscillation, and the error bar size increasing as predicted, up to $T_R \approx 300 \mu\text{s}$, where the size of the error bars starts to decay due to decoherence. In most circumstances the fitting of a model is applied only to the mean of the data, but here our main interest is shot-to-shot noise, so we use the model to fit also the standard deviation of the data (the size of error bars) as shown in Fig. A.5b. Since the main source for shot-to-shot fluctuations in our Ramsey sequence is magnetic field noise, we can write $\sigma_{\delta\omega} = 2\pi f_0 \frac{\Delta B}{B}$ and use the magnetic bias field stability $\frac{\Delta B}{B}$ as the fourth free parameter instead of $\sigma_{\delta\omega}$. The best fit between the data and the model in Fig. A.5 yields a field stability of $\frac{\Delta B}{B} \approx 3 \cdot 10^{-5}$.

To validate the optimization of the free parameters we plot R^2 as a function of the field stability in Fig. A.6. The maximal value of R^2 is 0.7 at $\frac{\Delta B}{B} = 3 \cdot 10^{-5}$. This result assures us that our power supply is operating well in terms of stability. According to this result, we should expect reasonably stable and visible Ramsey oscillations up to a Ramsey time of $T_R \approx 200 \mu\text{s}$.

To conclude, we have demonstrated a method to experimentally estimate the magnetic bias field stability by measuring the population vs. Ramsey time, and fitting a numerical simulation to the data. This method proved to be extremely beneficial, in terms of estimating the phase noise

¹We emphasize the distinction between the decoherence in the Ramsey sequence which affects the coherence of the superposition in each single shot and arises from coupling to the environment, and the shot-to-shot noise which doesn't affect the coherence of the superposition and will only cause smearing of the averaged population when averaging over several shots.

and shot-to-shot stability of the experimental parameters. The measurement also gives information regarding the Ramsey coherence time and the uncertainty in population per Ramsey interrogation time. The increasing size of error bars as a function of T_R indicates that the source of shot-to-shot phase noise is mainly fluctuations of the detuning, arising from magnetic bias field fluctuations. Fitting the data to the numerical simulation provided quantitative information regarding the stability of this field, which is not easy to obtain in other ways.

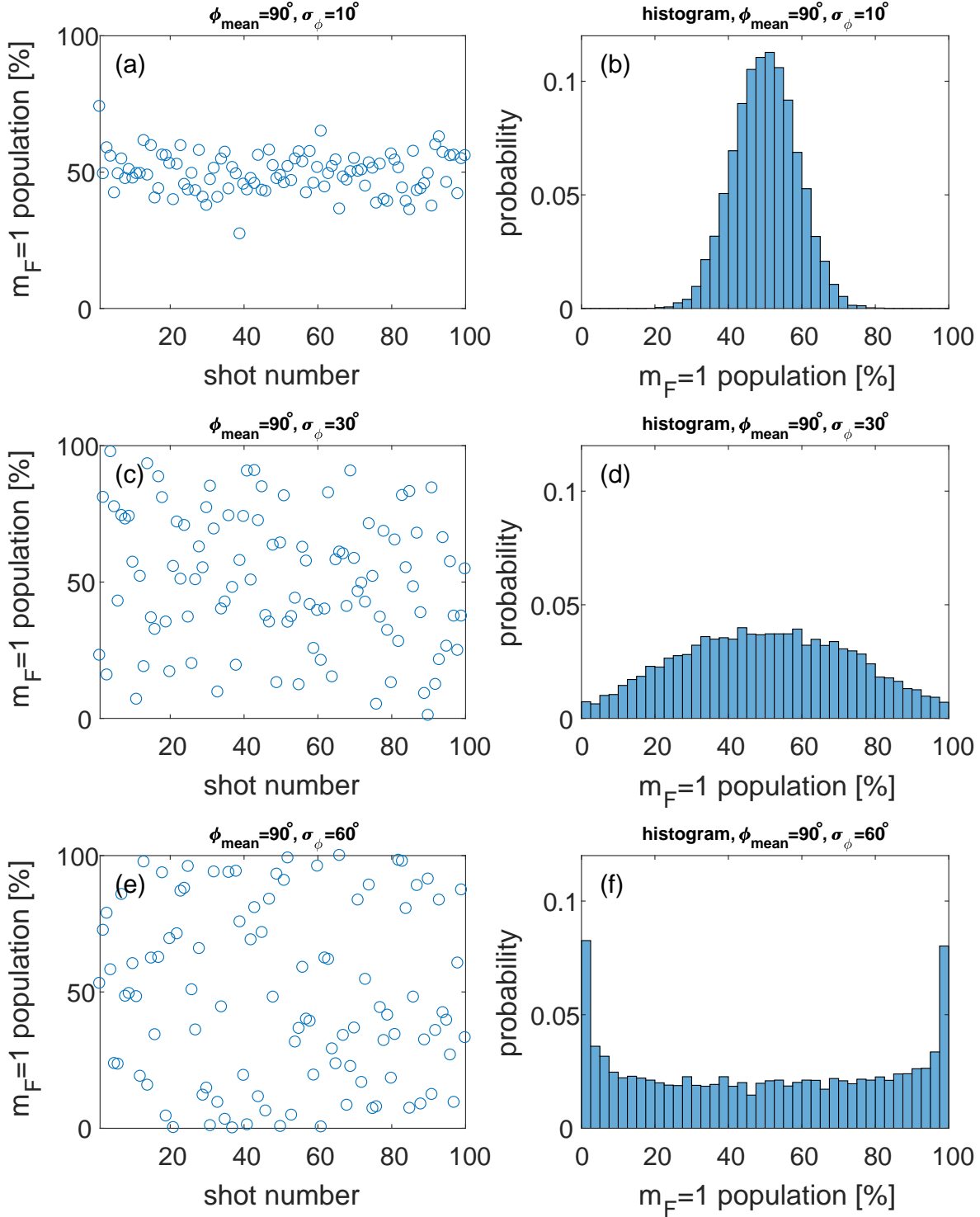


Figure A.2: Simulated shot-to-shot phase fluctuations. (a,c,e) Scatter plot for $\sigma_\phi = 10^\circ, 30^\circ, 60^\circ$, where $\phi_{\text{mean}} = 90^\circ$ corresponding to $P_{\text{mean}} = 0.5$. One can see that a phase noise of $\sigma_\phi = 30^\circ$ already leads to a scatter of population over the entire range from 0% – 100%. (b,d,f) The histogram of each set. Notice the shape of the histogram: (b) For small phase noise ($\sigma_\phi = 10^\circ$) the histogram resembles a Gaussian distribution. (d) The histogram for $\sigma_\phi = 30^\circ$ shows a wider Gaussian that approaches a uniform distribution, and for $\sigma_\phi = 60^\circ$ (f) we see a “bowl shape”, where this shape is due to the sinusoidal nature of the population, yielding bunching at the edges where the slope of the sinusoidal function is minimal. The bunching at the edges of the histogram is a clear signature of phase noise.

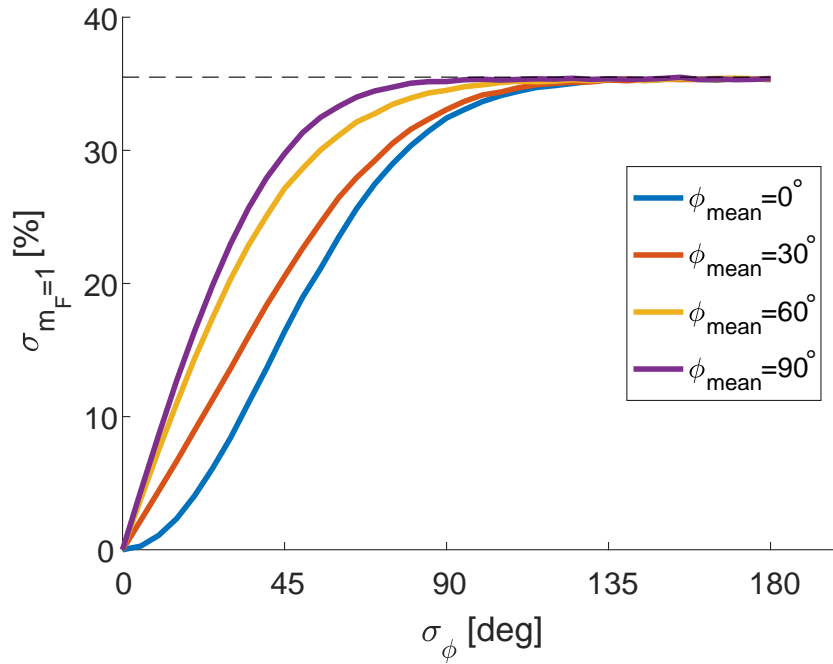


Figure A.3: Noise in population vs. phase noise (σ_P vs. σ_ϕ), numerical simulation. Plotted for $\phi_{\text{mean}} = 0^\circ, 30^\circ, 60^\circ, 90^\circ$, (corresponding to $P_{\text{mean}} = 0\%, 7\%, 25\%, 50\%$). σ_P starts with a linear relation to σ_ϕ and later reaches an asymptote with a maximal value of $\sigma_P \approx 35\%$. Using this plot and the experimental value of P_{mean} and σ_P one can extract the value of σ_ϕ . For large phase noise ($\sigma_\phi > 60^\circ$) this method loses its efficiency as σ_P approaches the asymptote.

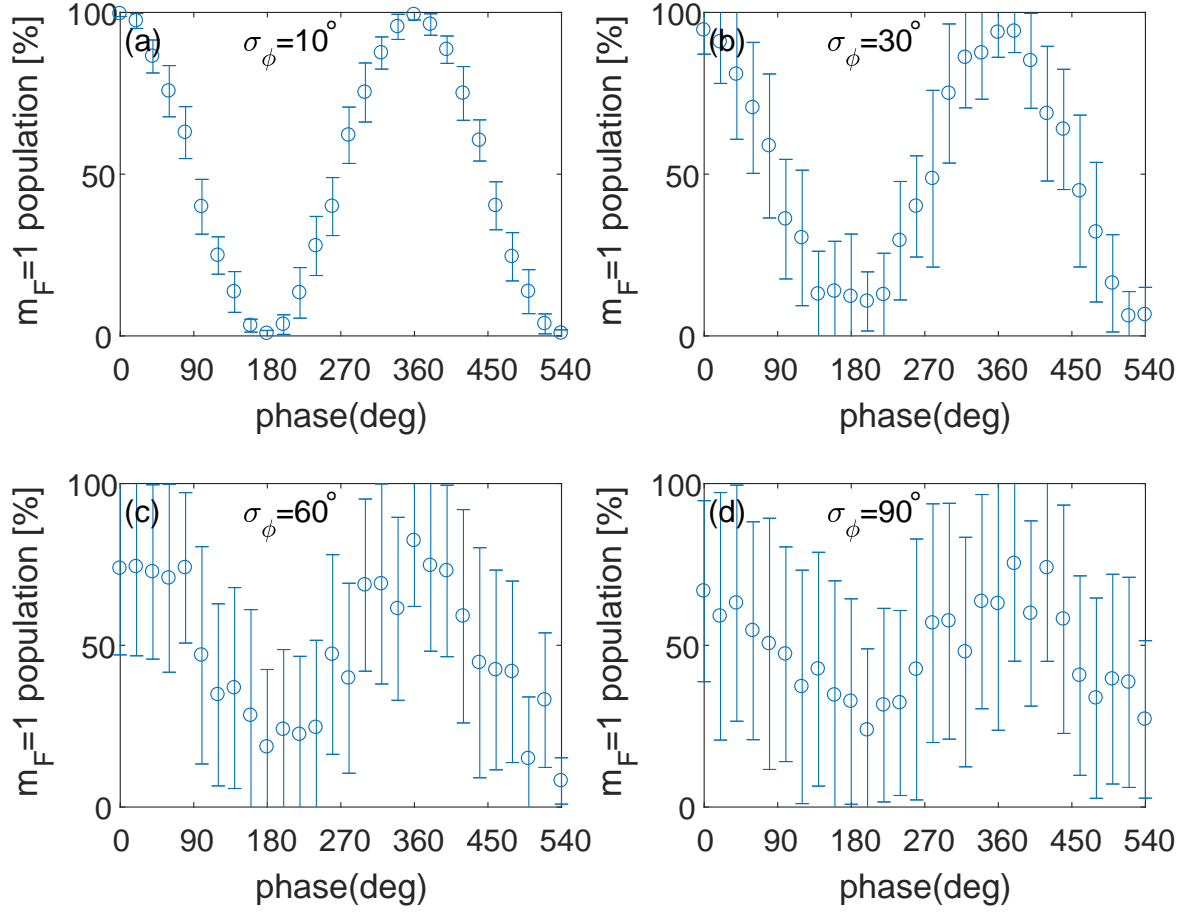


Figure A.4: Phase scan with shot-to-shot phase noise, 20 repetitions per data point, numerical simulation. Four plots showing a phase scan with different noise amplitude, $\sigma_\phi = 10^\circ, 30^\circ, 60^\circ, 90^\circ$. The shot-to-shot phase noise has two effects. First, it lowers the visibility of the population oscillation. Second, the size of the error bars oscillate along the scan, but this only happens if the phase noise is not “too big”. For a phase noise of $\sigma_\phi = 90^\circ$ the error bars do not significantly change along the phase scan since they are at the asymptotic regions shown in Fig. A.3. One can estimate the phase noise from such a measurement, but this approach will only be beneficial for rather small phase noise, since for $\sigma_\phi = 30^\circ$ it already requires a fine phase scan with a large number of repetitions per point to get a valid estimation.

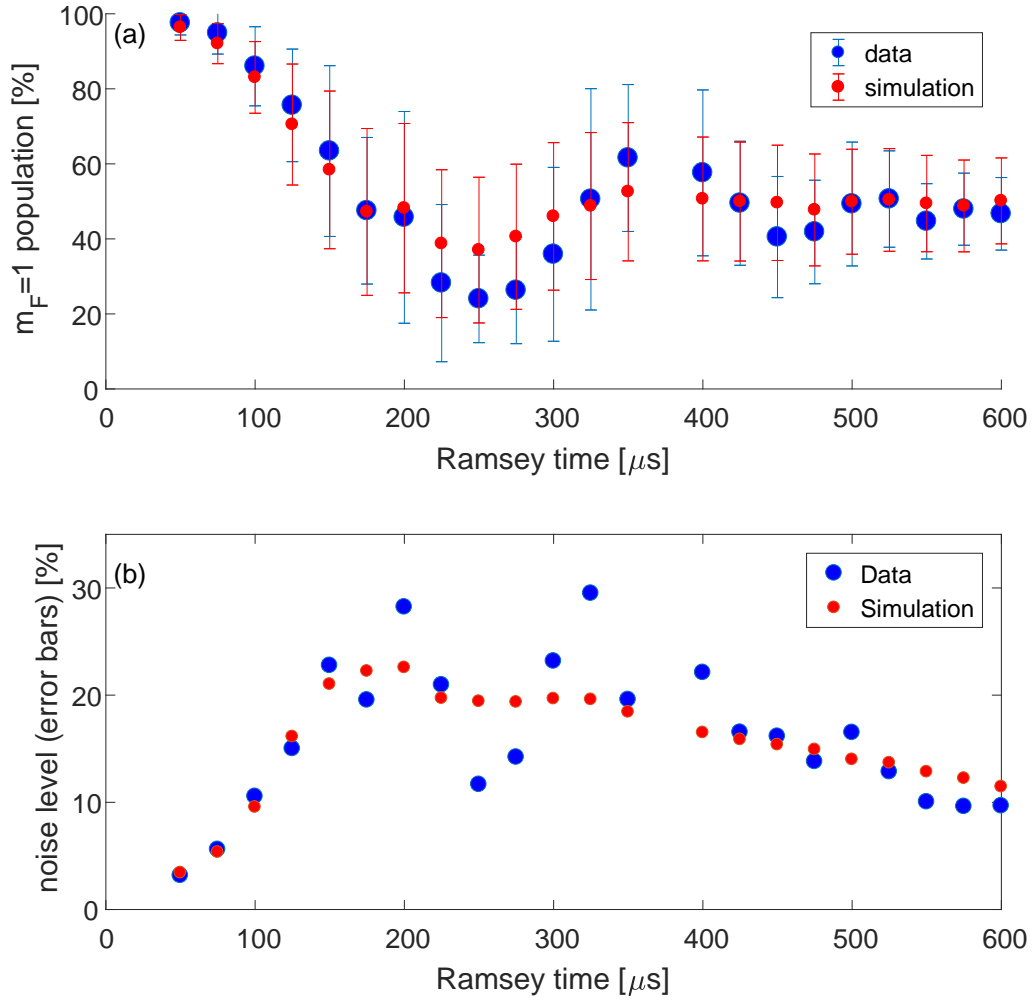


Figure A.5: Population vs. Ramsey time, experimental data vs. numerical simulation. The data exhibit a decaying population oscillation and the standard deviation of the data (size of the error bars) increases with increasing T_R , up to $T_R \approx 300 \mu\text{s}$, and later it decays as it becomes dominated by the decoherence (at $T_R \rightarrow \infty$ the population will decay to 50% and the size of the error bars will go to zero due to the decoherence). The model used here is a decaying oscillation with normally distributed phase noise. The population in the $m_F = 1$ state is given by $P(m_F = 1) = 0.5 + 0.5 \exp\left(-\frac{t}{\tau_R}\right) \cos[\delta\omega \times T_R + \phi_0]$ where $\delta\omega$ is normally distributed with $\delta\omega_{\text{mean}} = 2\pi(f_{\text{RF}} - f_0)$ and $\sigma_{\delta\omega} = 2\pi f_0 \frac{\Delta B}{B}$. For each value of T_R the simulation produces 300 values of $\delta\omega$, calculates the population for each of these $\delta\omega$, and then calculates the mean population and the standard deviation of the population for this value of T_R . This numerical simulation has 4 free parameters: $\delta\omega$, ϕ_0 , τ_R , and the stability of the magnetic bias field $\frac{\Delta B}{B}$. The detuning and initial phase determine the oscillation frequency and phase, while the decay rate and field stability determine the visibility of the oscillation and the standard deviation for each value of T_R (size of the error bars). The free parameters are first calibrated by hand to get a reasonable fit, and then optimized by a machine learning optimization algorithm [16]. This method estimates that the magnetic field stability in our experiment is $\frac{\Delta B}{B} = 3 \cdot 10^{-5}$, and $\delta\omega = 2\pi \times 1.7 \text{ kHz}$, $\tau = 540 \mu\text{s}$, and $\phi_0 = 4.8 \text{ rad}$. One can notice an interesting pattern in the noise level of the data [blue dots in (b)] from $t \approx 150$ to $t \approx 350 \mu\text{s}$ that does not appear in the simulation [red dots in (b)]. This fluctuating error bar size is explained by the fact that in the experimental data each point is an average of only 5 repetitions per point while in the simulation 300 repetitions are averaged per point. Performing the simulation with 5 repetitions shows a similar, more random, behavior. It should be noted that what is observed here are not the phase error oscillations shown in Fig. A.4a, since for $T_R = 225 \mu\text{s}$, we get $\sigma_\phi = 2\pi f_0 \frac{\Delta B}{B} T_R = 1.04 \text{ rad} \approx 60^\circ$.

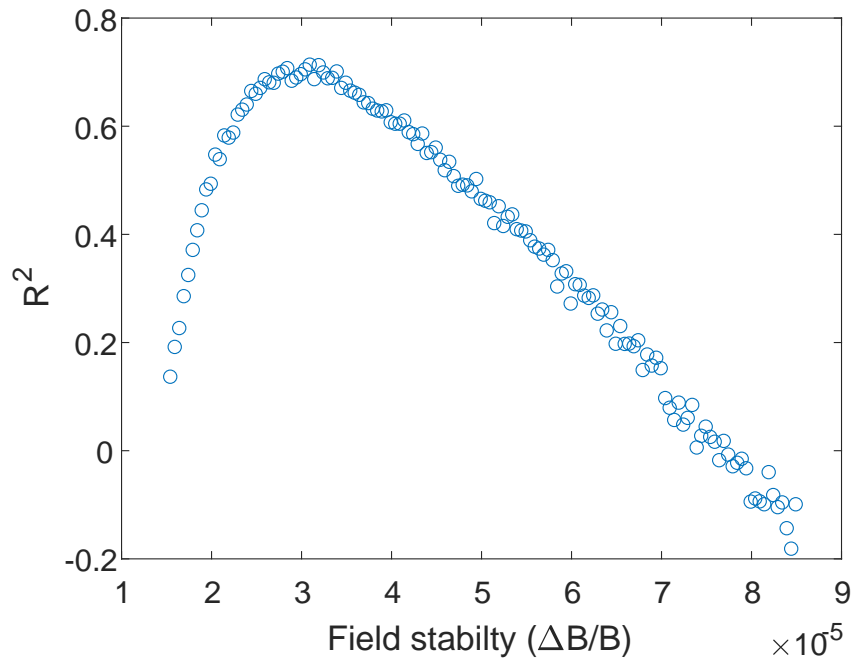


Figure A.6: Goodness of fit of the numerical simulation to the data in Fig. A.5b, as a function of the magnetic bias field stability $\frac{\Delta B}{B}$. The fitting is optimal for $\frac{\Delta B}{B} = 3 \cdot 10^{-5}$ with an $R^2 = 0.7$.

תקציר

אינטרפרומטרים מהווים חלק חיוני מהחקירה המדעית את הטבע והתופעות הפיסיקליות מזה זמן רב. דוגמאות לאינטרפרומטרים אופטיים מפורסמים הן למשל ניסוי שני הסדקים של יאנג, אשר חקר את ההתנהגות הגלית של האור, ניסוי מייקלסון מורלי, וההמשכה האולטימטיבית שלו בתקופתנו "אינטרפרומטר הלייזר לתצפית בגלי כבידה" (LIGO). אינטרפרומטרים אטומים פותחו לראשונה בשנות ה-90, וכיום הם כלי נפוץ במחקר בתחום מכניקת הקוונטים, וכמו כן משמשים למדידות מדויקות של כבידה וקבועים יסודיים, למדידה תאוצה במערכות ניווט אינרציאליות, ועוד. בעוד מרבית האינטרפרומטרים האטומיים עושים שימוש בהעברת התנע המסופקת על ידי פולסי לייזר כדי לשלוט באופן קוהרנטי במסלולי האטומים, אנחנו מבצעים משימה זו בעזרת גרדיאנטים מגנטיים הנובעים מזרמים בשבב אטומי. בתזה זו אני מציג את המימוש החלוצי שלנו לאינטרפרומטר שטרן-גרלך, בו הפיצול והאיחוד של חבילות הגל הקוונטיות מבוצע על ידי כוחות מגנטיים המגיעים מהאינטראקציה של הגרדיאנט המגנטי עם רמות זימן האטומיות.

אפקט שטרן-גרלך, אשר התגלה לפני כמאה שנה, הפך לפרדיגמה בתורת הקוונטים. באופן מפתיע כמעט ואין עדויות כי במערכת המקורית בה אטומים נעים באופן חופשי ונחשפים לגריאנטים מגנטיים, המגיעים ממגנטים מקרוסקופיים, נשמרת הקוהרנטיות הקוונטית. בנוסף, מספר מחקרים תיאורטיים הסבירו בעבר מדוע זהו אתגר קשה לביצוע. איחוד של חבילות הגל באינטרפרומטר שטרן-גרלך נדרש למעשה להיות פעולה הפוכה בזמן לפעולת הפיצול, באופן כזה ששני הגראדיאנטים האחרונים מבטלים לחלוטין את הפעולה של שני הגרדיאנטים הראשונים. על מנת להשיג קוהרנטיות גבוהה (או ניגודיות גבוהה) בפלט של אינטרפרומטר עם פיצול מרחבי, מוכרחים לבצע פעולות מדויקות ויציבות על האטומים באופן כזה שהמרחק הסופי בין חבילות הגל יהיה מינמלי, והמהירות היחסית הסופית תהיה מינמלית גם כן. כל סטייה מחפיפה מושלמת במיקום או במהירות יגרום לדעיכה של ניגודיות האינטרפרומטר. בעוד ששמירה על דיוק היא האתגר העיקרי שלנו, עלינו לעמוד גם בדרישה של יציבות הפעולות בין ניסוי לניסוי, שכן תנודות אקראיות של הפרמטרים הניסיוניים (למשל השדה המגנטי האחד) ישפיעו על הפאזה של הניסוי, או במקרה של אי יציבות בגרדיאנטים המגנטיים ימנעו איחוד של חבילות הגל.

בפרק 1 של התזה אני מתאר את מערכת הניסוי הנמצאת במעבדה שלנו, ואת השינויים שערכנו בה במהלך עבודה זו.

פרק 2 מתאר את ההליך הניסיוני על מנת להגיע לעיבוי בוז-איינשטיין, והצעדים הראשוניים הדרושים למניפולציה של האטומים על מנת להגשים את האינטרפרומטר.

בפרק 3 מוצג הרקע התיאורטי של אינטרפרומטריה אטומית, בדגש על הניגודיות והפאזה של אינטרפרומטר שטרן-גרלך.

פרק 4 מציג את המימוש שלנו לאינטרפרומטר שטרן-גרלך, עם תוצאות המאשרות את האיחוד המוצלח של חבילות הגל על ידי שני הגראדיאנטים האחרונים. אנו גם מאששים את הצפי התיאורטי עבור הפאזה באינטרפרומטר שטרן-גרלך, והתלות של פאזה זו בהפרדה המרחבית הסופית של חבילות הגל. לבסוף אנו מציגים מדידה של אורך הקוהרנטיות של חבילת הגל באינטרפרומטר שלנו.

בנספח A אנו דנים בהשפעה של תנודות אקראיות בפאזה בין ניסוי לניסוי על האות הניסיוני, ומציעים הליך להערכה של מקורות הרעש המשפיעים על יציבות הפאזה.

אוניברסיטת בן-גוריון בנגב
הפקולטה למדעי הטבע
המחלקה לפיסיקה

קוהרנטיות באינטרפרומטר שטרן-גרלך

חיבור זה מהווה חלק מהדרישות לקבלת התואר "מוסמך למדעי טבע" (M.Sc.)

מאת: אור דובקובסקי
בהנחיית: פרופסור רון פולמן

30.9.2020
תאריך: _____

30.9.2020
תאריך: _____

תאריך: _____

אור

חתימת הסטודנט: _____

Dr. Ron Folman
Ajam Chip Group
Ben-Gurion Uni.

חתימת המנחה: _____

חתימת יו"ר הועדה המחלקתית: _____

ספטמבר 2020

אוניברסיטת בן-גוריון בנגב
הפקולטה למדעי הטבע
המחלקה לפיסיקה

קוהרנטיות באינטרפרומטר שטרן-גרלך

חיבור לשם קבלת התואר "מגיסטר" בפקולטה למדעי הטבע

מאת: אור דובקובסקי
בהנחיית: פרופסור רון פולמן